POLITECNICO DI MILANO

School of Industrial and Information Engineering
Master of Science in Biomedical Engineering

DEVELOPMENT OF AN ELECTRONIC NOSE FOR THE DETECTION OF LUNG CANCER BIOMARKERS IN EXHALED BREATH

Supervisor: Pietro Cerveri
Co-Supervisor: Davide Marzorati

Thesis of:
Andrea Rescalli
Student ID: 943239

Academic Year 2020-2021

A ciò che è stato,
A ciò che ancora non è.

Abstract

In 2020, 18% of the 9.96 million recorded deaths for cancer was due to lung cancer. This pathology can occur in different forms depending on the cells it originates from, and the most adequate treatment (typically chemotherapy, radiotherapy or surgical intervention) varies according to the nature of the tumor. The efficacy of the treatment, and consequently the survivability rate of the patient, is higher when the tumor is diagnosed in its early stages (I or II), but usually symptoms related to lung cancer occur in more advanced stages of the disease (III or IV), or they are mistaken for symptomatology caused by other pathologies, such as chronic obstructive pulmonary disease. It is then of crucial importance to have screening tools able to perform a preventive audit on a high-risk population to identify asymptomatic patients and direct them towards diagnostic exams (more expensive and invasive), with the aim of intervening as early as possible on the neoplasia and increasing the patient chances of survivability.
At the moment, screening programs are based on imaging techniques such as low-dose computed tomography which, despite the reduction in terms of patient radiation exposure with respect to standard computed tomography, still remains an invasive technique and produces a high number of false positives. To overcome these limitations, in the last years new solutions have been explored, amongst which there is exhaled breath analysis: a non-invasive technique that, by the study of the volatile organic compounds contained in the patient exhaled air, is capable of distinguishing amongst them the presence of specific biomarkers, which are indicators of the disease occurrence. The technologies that are commonly used to carry out this type of analysis are gas chromatography and mass spectrometry, which offer high accuracy but at the same time are expensive and complex. Recently, innovative technologies based on sensor arrays, electronic noses, have begun to develop: these are small, portable and moderately priced devices, able to analyze the content of a gas sample in real time and react to the presence of certain biomarkers.
The purpose of this thesis was to create a device based on polymeric sensors capable of recognizing, with sufficient accuracy and selectivity, three different volatile organic compounds (i.e. toluene, butanone and hexanal) present in three distinct gas mixtures, in a closed environment and in static conditions. This is a preliminary work with the aim of developing a system that can be applied in the future, within the context of lung cancer screening, to samples of exhaled air. The created system mainly consists of three parts: the resistive and capacitive biosensors, made by the team of Professor Francesco Cellesi and Francesco Bosatelli by exploiting the deposition of thin films of molecularly imprinted polymers on interdigitated electrodes; an electronic circuit, entirely driven by a microcontroller, for the acquisition and processing of the signal; a graphic interface developed in order to allow the user to interact dynamically with the device and visualize the acquired data.
From the validation tests performed, the developed device has shown performances comparable to those of the instruments used as a reference (in some cases even better), in particular for resistive measurements. It was then used in the laboratory to investigate the behavior of

(resistive) sensors after being exposed to each of the three compounds under examination. Each sensor showed a response, in terms of resistance variation with respect to the baseline value, to each of the compounds it came into contact with, showing a poor selectivity; however, the induced response was different from compound to compound. This is an excellent result, which paves the way for the possible use of these sensors in combination with artificial intelligence algorithms to distinguish the presence of certain compounds in gas samples of unknown composition. Furthermore, experiments on the intensity of the response as a function of the exposure time have shown how the more the sensor has been in contact with the compound under exam, the more accentuated the variation in resistance with respect to the baseline is.

The work carried out in this project represents only the first step towards the development of a lung cancer screening tool that can be effectively applied in a clinical setting; still, the results turned out to be very promising.

Sommario

Nel 2020, il 18% delle 9,96 milioni di morti per tumore è stata causata da tumore al polmone. Questa patologia si può manifestare sotto diverse forme, dipendentemente dalle cellule dalle quali origina, e il trattamento terapeutico più adeguato (tipicamente chemioterapia, radioterapia o asportazione chirurgica) varia in base alla natura del tumore. L'efficacia del trattamento, e di conseguenza la probabilità di sopravvivenza del paziente, è più elevata quando il tumore viene diagnosticato in uno stadio precoce (I o II), ma la maggior parte dei sintomi legati al cancro al polmone si manifesta negli stadi più avanzati della malattia (III e IV), oppure viene confusa con sintomatologia dovuta ad altre patologie (come ad esempio la broncopneumopatia cronica ostruttiva). È dunque di importanza fondamentale disporre di strumenti di screening in grado di effettuare un controllo preventivo sulla popolazione ad alto rischio per identificare eventuali pazienti asintomatici e indirizzarli verso successivi esami diagnostici (più costosi e invasivi), al fine di intervenire il prima possibile sulla neoplasia e aumentare la probabilità di sopravvivenza del paziente.
Attualmente, i programmi di screening si basano su tecniche di imaging come la tomografia computerizzata a bassa dose, che pur riducendo il quantitativo di radiazioni a cui viene sottoposto il paziente rispetto ad una tomografia tradizionale, resta comunque una tecnica invasiva e produce un elevato numero di falsi positivi. Per far fronte a queste limitazioni, negli ultimi anni sono state esplorate nuove soluzioni, tra le quali l'analisi del respiro esalato: si tratta di una tecnica assolutamente non invasiva che, attraverso lo studio dei composti volatili organici dispersi nell'aria espirata dal paziente, è in grado di distinguere tra di essi specifici biomarcatori, indicatori della presenza della malattia. Le tecnologie che comunemente vengono impiegate per effettuare questo tipo di analisi sono la gascromatografia e la spettrometria di massa, le quali offrono elevata accuratezza ma al tempo stesso sono costose e complesse. Recentemente hanno cominciato a svilupparsi tecnologie innovative basate su array di sensori, i nasi elettronici: si tratta di dispositivi di piccole dimensioni, portabili e con prezzi moderati, in grado di analizzare anche in tempo reale il contenuto di un campione di gas e reagire alla presenza di determinati biomarcatori.
Lo scopo di questa tesi è stato quello di realizzare un dispositivo basato su sensori polimerici in grado di riconoscere, con sufficiente accuratezza e selettività, tre differenti composti volatili organici (toluene, butanone ed esanale) presenti in tre distinte miscele gassose, in un ambiente chiuso e in condizioni statiche. Si tratta di un lavoro preliminare con lo scopo di sviluppare un sistema che possa essere in futuro applicato, in un contesto di screening per il tumore al polmone, a campioni di aria esalata. Il sistema realizzato si compone principalmente di tre parti: i biosensori resistivi e capacitivi, realizzati dal team del Professor Francesco Cellesi e Francesco Bosatelli sfruttando la deposizione di film sottili di polimeri a stampo molecolare su elettrodi interdigitati; un circuito elettronico di acquisizione ed elaborazione del segnale interamente pilotato da microcontrollore; un'interfaccia grafica con lo scopo di permettere all'utente di interagire dinamicamente col dispositivo e visualizzare i dati acquisiti.
Dai test di validazione eseguiti, il dispositivo sviluppato ha dimostrato performances compa-

rabili a quelle degli strumenti usati come riferimento (in alcuni casi addirittura migliori), in particolare per quanto riguarda le misure di resistenza. È stato quindi utilizzato in laboratorio per indagare il comportamento dei sensori (resistivi) in seguito all'esposizione a ciascuno dei tre composti in esame. Ciascun sensore ha mostrato una risposta, in termini di variazione di resistenza rispetto al valore di baseline, ad ognuno dei composti coi quali è entrato in contatto, evidenziando una scarsa selettività; tuttavia, la risposta si è rivelata differente da composto a composto. Questo è un ottimo risultato, che apre la strada al possibile utilizzo di questi sensori in combinazione con algoritmi di intelligenza artificiale per distinguere la presenza di determinati composti in campioni gassosi dalla composizione ignota. Inoltre, esperimenti sull'intensità della risposta in funzione del tempo di esposizione hanno evidenziato come la variazione di resistenza rispetto alla baseline sia tanto più accentuata quanto più il sensore è stato a contatto con il composto in esame.
Il lavoro svolto in questo progetto rappresenta solo il primo passo verso lo sviluppo di uno strumento di screening per il cancro al polmone che possa essere effettivamente applicato in un contesto clinico; tuttavia, i risultati si sono rivelati promettenti.

Contents

List of Figures

List of Tables

List of Abbreviations

BODS Bis(2-methacrylol)OxyethylDiSulphide

BuMA Butyl MethAcrylate

BzMA Benzyl MethAcrylate

CAD Computer-Aided Detection

ChMA Cyclohexyl MethAcrylate

COPD Chronic Obstructive Pulmonary Disease

CT Computed Tomography

CXR Chest X-Ray

DANTE Detection And screening of early lung cancer with Novel imaging TEchnology

DLCST Danish Lung Cancer Screening Trial

EBA Exhaled Breath Analysis

EBC Exhaled Breath Condensate

GC Gas Chromatography

GUI Graphical User Interface

IDE InterDigitated Electrodes

IDE Integrated Design Environment

IMS Ion-Mobility Spectrometry

IUPAC International Union of Pure and Applied Chemistry

LC Lung Cancer

LDCT Low-Dose Computed Tomography

Lung-RADS Lung Imaging Reporting And Data System

MAA MethAcrylic Acid

MIPs Molecularly Imprinted Polymers

MS Mass Spectrometry

NIP Non-Imprinted Polymer

NLST National Lung Screening Trial

NSCLCs Non-Small Cell Lung Cancer

OSHA Occupational Safety and Health Administration

PCB Printed Circuit Board

PLA Polylactic Acid

PLCO Prostate, Lung, Colorectal and Ovarian Cancer

PSoC Programmable System on Chip

PTR Proton Tranfer Reaction

RCT Randomized Controlled Trial

SCLCs Small Cell Lung Cancer

SERS Surface-Enhanced Raman Scattering

SESI Secondary Electron-Spray Ionization

SPR Surface Plasmon Resonance

SqCCs Squamous Cell Carcinomas

VOCs Volatile Organic Compounds

Chapter 1

Introduction

Cancer is one of the leading causes of death globally, resulting in almost 10 million people dying only in 2020. In the last year, with a total number of new cases grown beyond 19 millions, the most common cancer types detected were breast (2.26 million cases, 11.7%), lung (2.21 million cases, 11.4%) and colon and rectum (1.93 million cases, 10%). By looking at mortality data, lung cancer is at the top of the table, being responsible for 18% of the 9.96 million recorded deaths for cancer [1].

Lung Cancer (LC) is a tumor of lung tissue that can be classified differently according to its histopathological profile [2, 3, 4]. In particular, it is possible to differentiate between:

- Non-Small Cell Lung Cancer (NSCLCs), representing 80 to 85% of all cases. It can be further divided into adenocarcinomas, squamous cell carcinomas and large cell carcinomas. These subtypes originate from different types of lung cells but their treatment and prognosis are often similar.
  - Adenocarcinomas: arise from epithelial cells in charge of the secretion of substances such as mucus. They occur mainly in current or former smokers (even if they are the most common LC type in non-smokers); women are more subjected than men to these forms of LC and they are more likely to occur in younger people if compared to the other types. Adenocarcinomas usually originate in the outer parts of the lung.
  - Squamous Cell Carcinomas (SqCCs): arise from surface epithelial cells, squamous cells, which line the inside of the airways in the lungs. They are mainly linked to a smoking history and develop from the central part of the lungs, near a main airway.
  - Large Cell Carcinomas: also called undifferentiated carcinoma, can appear in any part of the lung and are diagnosed when histology cannot be referred to any other type of cancer. They have a tendency to grow and spread quickly.
- Small Cell Lung Cancer (SCLCs), representing 10 to 15% of all cases. Their origin is not fully understood yet, but are commonly thought to arise from neuroendocrine cells in the lung epithelium.

- Others: aside the two main types of LC, more rare pathologies such as lung carcinoid tumors and adenoid cystic carcinomas, lymphomas, and sarcomas can be found.

Treatment is strongly dependent on the type of LC. SCLCs are fast growing tumors; for this reason, they tend to respond quite well to chemotherapy or radiation treatment. On the other hand, in a patient diagnosed with NSCLC it is more common to proceed with a surgical intervention, due to the fact that this type of tumor grows slowly and chances are that has not spread yet at the time of treatment.

Early identification of cancer is crucial for increasing responsiveness to effective treatments, improving chances of survivability and reducing the overall cost of the treatment care. Data for NSCLCs assess that surgical resection for small, localized tumors identified in the earliest stage (stage I) offers a favourable prognosis, with 5-years survival rate between 70 and 90% [5]; by looking at the latest information published by the UK Office for National Statistics for the 2012-2015 period, 1-year survival rates for lung cancer diagnosed at stage I oscillate between 79 to 91%, whereas for stage III are between 41 and 52% and between 14 to 21% in case of stage IV detection [6].
SCLCs, as already said, are more aggressive; therefore they are characterized by lower survival rates, and they are more likely to be diagnosed at later stages. Overall 5-years survival rate can drop down to 5% [5], but for early diagnosis of SCLC there is the possibility of intervention with high benefits: according to a study published in 2016 by Yang *et al.* 5-years survival rate can go from 40% with resection only up to 52% for resection in conjunction with adjuvant chemotherapy [7].
It should now be evident the importance of early detection. To achieve this objective, two main strategies can be adopted:

- Early diagnosis: early identification of cancer in *symptomatic* patients. Its utmost goal is to discover the disease as early as possible to proceed with diagnosis and treatment without delay (the earlier the intervention, the higher the survival rate);

- Screening: identification of unrecognized (pre-clinical) cancer or pre-cancerous lesions in *asymptomatic* and apparently healthy target population. This can be achieved by means of tests, examinations, imaging techniques or other procedures aiming at finding cancer biomarkers in biological fluids, such as blood, urine, and exhaled breath. In screening protocols, an entire population is evaluated: the majority of tested people will not have the disease. Limiting the number of false positives (healthy people erroneously diagnosed with the disease) is crucial to avoid unnecessary costs for invasive diagnostic follow-ups.

Table 1.1 briefly summarizes the main aspects and differences between early diagnosis and screening exposed in the *'Guide to Cancer Early Diagnosis'* published by the World Health Organization [8].
Lung cancer, in its early stages, is either asymptomatic or characterized by symptoms that can be connected to other respiratory pathologies. For this reason, it is more cost-effective and more beneficial for the patient's health to focus on screening programs for early detection, rather than on early diagnosis ones.

The aim of this thesis is to develop an electronic device based on polymeric biosensors for the recognition of specific organic compounds in a gaseous environment, for future application to exhaled breath samples. The compounds under analysis are toluene, butanone and hexanal: a thorough literature research revealed them as some amongst the most frequent

Table 1.1: *Main elements of early diagnosis and screening.*

Parameter	Early diagnosis	Screening
Number of participants	Symptomatic population.	Entire target population.
Test	Diagnostic test for symptomatic patients.	Screening test for entire target population with diagnostic test only for those screened positive.
Public awareness	Attention to signs and symptoms.	Attention to signs and symptoms and participation to screening programs.
Potential benefits	Reduction in staging of the disease at diagnosis; Higher survival rate if combined with treatment.	Potential reduction in incidence when a precursor is detected; Reduction in staging of the disease at diagnosis; Higher survival rate if combined with treatment.
Potential risk	Low: Only performed on symptomatic people.	High: Radiation exposure; False positives can induce an increase in costs for future tests, and can have impact on psychology of the subject; False negatives can lead to underestimation of future symptoms.

organic compounds found in the exhaled breath of subjects affected by lung cancer; hence, they could be considered as possible biomarkers in lung cancer screening applications.
The work of this projects focuses mainly on three parts:

- A chemical part, which consists in the realization of the biosensors aimed at recognizing the target analytes. This part has been carried out by the team of Professor Francesco Cellesi and Francesco Bosatelli at Politecnico di Milano's Applied Physical Chemistry Lab (Department of Chemistry, Materials and Chemical Engineering 'Giulio Natta'). They developed both capacitive and resistive thin-film Molecularly Imprinted Polymers (MIPs) sensible to each one of the three analyte taken into consideration; these films have been deposited onto gold InterDigitated Electrodes (IDE) produced by MicruX Technologies whose purpose is to convert the changes in the polymer's properties upon target recognition into an electrical signal than can be acquired.

- An electronic part, devoted to the readout of the signals generated by the biosensors. The whole system is entirely based on a microcontroller, the CY8CKIT-059 PSoC 5LP Prototyping Kit by Cypress Semiconductor Corporation. The firmware has been developed inside *PSoC Creator*, the Cypress' dedicated Integrated Design Environment (IDE), and enables the PSoC 5LP to perform both capacitive and resistive measurements, as well as to communicate with an external host machine. A Printed Circuit

Board (PCB) and a 3D printed custom case have been designed with Autodesk EAGLE and Autodesk Fusion 360 respectively to facilitate the connection between the circuitry and the biosensors.

- A software part, concerning the development of a Graphical User Interface (GUI). This application has been realized with Python exploiting the PyQt5 library, and allows the user to manage the acquisitions, visualize the data acquired, and even export them in a separate file for further processing.

The capacitive and resistive circuits have been tested to assess their performances, and eventually employed in a laboratory environment. A detailed description of both solutions will be provided, but the results will focus only on the resistive part.

The manuscript of this thesis is structured as follows:

- Chapter 2 introduces the reader to the state of the art, guiding him through a brief overview of the main screening tools for lung cancer, focusing in particular on Exhaled Breath Analysis (EBA) and electronic noses; finally, MIPs and their employment in biosensors are covered.
- Chapter 3 illustrates the theoretical principles involved in the realization of this project, and the technological solutions adopted to exploit them; it gives a detailed description of the steps followed during the preparation of the imprinted polymers, the materials employed and the developed firmware and software code.
- Chapter 4 focuses on presenting the testing phase that has been performed to validate the developed device, the acquisition protocol adopted during the laboratory measurement sessions and finally the results obtained.
- Chapter 5 concludes the treatise with a general discussion on the project, a comment on the results presented in the previous chapter and a final note regarding limitations and possible future developments.

Chapter 2

State of the Art

Within the context of screening and early detection of lung cancer, the state of the art techniques now be presented, alongside relevant information for a more exhaustive comprehension of the whole discussion.

2.1 Traditional screening methods for lung cancer

Some people are more likely than others to develop lung cancer, and anything that enhances the probability of developing LC is called a risk factor. Known risk factors for LC are tobacco smoking, contact with radon, asbestos or other carcinogenic agents that target the lungs (such as arsenic, beryllium, cadmium), history of cancer (either personal or family related), history of lung diseases such as Chronic Obstructive Pulmonary Disease (COPD) or pulmonary fibrosis [9].
The gold standard measure of screening efficacy is its mortality reduction. This, combined with the non-negligible risks associated to LC screening, leads to an optimal target population composed only by individuals most at risk, in contrast with other population-based screening programmes like breast ones where all individuals (of a certain age and sex) are eligible. Nevertheless, most at risk individuals are usually the least likely to participate in these programmes, making their engagement a fundamental step in LC screening application. Amongst the most common reasons for non-participation in screening programmes there are travel, discomfort and costs [10]. Accessibility can be improved for example by exploiting mobile Computed Tomography (CT) scanners [11]; emotional aspects such as fear and anxiety can be addressed with information leaflets focusing more on the health check rather than on cancer detection; finally, new low-cost technologies can be adopted such as EBA, as it will be discussed in sections 2.2 and following.

2.1.1 Chest X-ray

During the 1970s and 1980s efforts were made to determine the efficacy of screening protocols relying on Chest X-Ray (CXR) with or without sputum cytology in reducing lung cancer mortality. The results of several studies demonstrated that screening led to earlier detection and improved survival rates, but none of them showed a reduction in mortality. In the Mayo [12] Randomized Controlled Trial (RCT), patients were divided into either an intensive-screening experimental group where sputum cytology and CXR were checked every 4 months

or a control group where the standard yearly screening was provided; no difference in mortality between the two groups was detected. In another RCT, the Johns Hopkins study [13], CXR screening protocol with or without sputum cytology was evaluated; no difference in mortality by addition of cytology was found.
Negative results from the early lung cancer screening RCTs could have been due to limitations in the early study designs. This led to further attempts to properly evaluate CXR, and in the 1990s the Prostate, Lung, Colorectal and Ovarian Cancer (PLCO) screening trial [14] was launched, where 150 000 patients were randomized into either annual CXR or usual care (i.e. no screening intervention). In agreement with the previous studies, no mortality benefit was found in CXR screening.
These findings, combined with the limited sensitivity of CXR (dependent on size and location of the lesion, image quality and technician interpretation), pushed researchers to explore newer imaging techniques.

2.1.2 Low-dose computed tomography

CT is considered a key imaging method in the investigation of lung diseases, empowering characterization of morphological lesions and measurement of nodule size (thus enabling nodule growth monitoring); moreover, being a 3D imaging technique, allows for the view along different sections. However, the average effective dose for a typical standard-dose chest CT (around 7 mSv/scan [15]) is considered to be too high for the benefits of early detection. Low-Dose Computed Tomography (LDCT) instead uses an average of 2 mSv/scan, thus reducing by over 70% the effective radiation dose provided to the patient, while still keeping sensitivity of small nodule detection unaltered [16].
Several studies, like the Detection And screening of early lung cancer with Novel imaging TEchnology (DANTE) [17, 18] and the Danish Lung Cancer Screening Trial (DLCST) [19] involving respectively 2472 and 4104 patients, have shown that LDCT screening had no impact on lung cancer mortality, despite the increased detection of early stage disease. Nevertheless, being LDCT such a powerful tool, it was postulated that these studies were underpowered; in fact, in 2011 the results of a much larger RCT were published: the National Lung Screening Trial (NLST), involving 53 454 participants at risk of lung cancer, randomized to annual LDCT screening group versus CXR screening group, and evaluated over 3 years, demonstrated that mortality from lung cancer with LDCT screening was reduced by 20% and death from any cause was reduced in the low-dose CT group, as compared with the radiography group, by 6.7% [20].

LDCT screening does not come without harms; a detailed risks versus benefits analysis is reported in Table 2.1. It is worth mentioning that one possible cause for false positives could be related to the substantial variation in lung nodule definition amongst radiologists [22]. To overcome this issue, the American College of Radiology has developed the Lung Imaging Reporting And Data System (Lung-RADS), a quality assurance tool designed to standardize lung cancer screening CT reporting, reduce confusion in lung cancer screening CT interpretations and facilitate outcome monitoring [23].
On the other hand, to reduce the number of false negatives caused by diagnostic errors, Computer-Aided Detection (CAD) systems can be implemented to assist the radiologists in nodule detection while also reducing the reading time of a CT scan and helping the differentiation between malignant and benign lesions. These tools have shown to improve performance of experts, but can be affected by several factors related both to scanning parameters (e.g. section thickness, dose) and nodule characteristics (e.g. size, shape, density, location). For these reasons, integration of CAD tools in clinical workstations is a challenging task and has

Table 2.1: *Risks versus benefits of a LDCT lung cancer screening.*

Risks	Benefits
Anxiety and psychological effects associated to test results.	Improvements in the quality of life by finding cancer early, which reduces mortality from LC and/or from LC treatments.
False positives: identification of benign, non-calcified nodules lead to unnecessary, expensive follow-ups and invasive diagnostic tests; False negatives: missed tumors. They can induce patients to ignore symptoms.	Follow-ups and annual tests can help find missed tumors.
High costs.	An early identified cancer saves money in the long run; People at high risk might have insurance policies (partially) covering some costs.
Exposure to radiation (not precisely quantifiable, highly dependent on type and generation of CT scanners).	LDCT uses very low levels of radiations, and technological improvements on the scanners make them safer and safer.
Overdiagnosis: detection of cancers that would not have contributed to the death of the patient because of competing causes of death or because the lesion is indolent, leading to overtreatment. Very difficult to be quantified.	Screening is performed only on subjects at high risk: group 1 (55 to 74 y.o. with more than 30 pack-years, quit smoking within the last 14 years or current smoker) and group 2 (50 y.o. or older with 20 pack-years and presence of other risk factors) [21].

not been efficiently accomplished yet [24].

2.2 Exhaled breath analysis

Given its benefits, LDCT at the moment is the principal technique employed in lung cancer screening programmes. Nevertheless, the aforementioned risks and limitations cannot be overlooked, and other techniques are progressively starting to be taken into consideration, such as the analysis of exhaled breath.

Exhaled breath is a mixture of different types of compounds that can be grouped into [25]:

- Inorganic compounds, e.g. carbon dioxyde, oxygen. They represent the biggest portion of exhaled breath;
- Non-volatile compounds, e.g. isoprostanes, leukotrienes, hydrogen peroxide. They are suspended liquid-phase particles that can be found in Exhaled Breath Condensate (EBC). EBC can be retrieved from exhaled breath by a process of cooling through contact with a cold surface, that allows vapour to condensate;
- Volatile Organic Compounds (VOCs), e.g. saturated hydrocarbons (ethane, aldehydes), unsaturated hydrocarbons (isoprene), oxygen-containing (acetone), sulfur-containing (dimethylsulfide) and nitrogen-containing (dimethylamine, ammonia) compounds [26].

Human exhaled breath contains a large variety of VOCs, whose concentration is limited to the part-per-billion or even part-per-trillion range.

2.2.1 Volatile organic compounds as biomarkers for lung cancer

VOCs are organic compounds characterized by relatively high vapour pressure or volatility, and can be classified into endogenous or exogenous depending on their origin. The former reflect the cellular processes and metabolic activities that occur at tissue level, from which VOCs are released into the bloodstream and reach skin, lungs, liver and kidneys and are eventually excreted; for this reason they can be found in the headspace of cancer cells (i.e. the gas environment trapped above the cells in a sealed vessel) or blood samples, sweat, urine, feces and/or in the exhaled breath [27]. The latter are produced by the external environment and introduced inside the body by inhalation or absorption (through lungs, skin, digestion processes); an example can be propanol, typically found in the breath of hospitalized patients due to its usage in disinfectants.
VOCs have shown clinical relevance in the diagnosis of several diseases such as infectious diseases, asthma, COPD, and their application to lung cancer screening has been investigated a lot in recent years. In fact, tumor growth is usually linked to gene and/or protein changes [28]. It has been shown that in lung cancer, enzymes belonging to the cytochrome p450 superfamily are overactivated (due to a combination of both genetic and external risk factors), leading to a modulation of the catabolism of endogenous VOCs products of oxidative stress, which results in an altered pattern of breath VOCs. Hydrocarbons (and alcohols, given their derivation from alkanes depends on cytochrome p450 enzymes activity), aldehydes and some ketones concentrations in exhaled breath are altered by this very biochemical pathway. Aromatic compounds are instead considered exogenous compounds associated with exposure to cigarette smoke, alcohol, pollution, and radiation; these molecules are highly reactive, and they can cause peroxidative damage to proteins and DNA, thus increasing chances of developing cancer; moreover, their presence in the human body induces enzymatic defense mechanisms, such as the activation of cytochrome p450 enzymes, which will once again modify the physiological profile of exhaled breath VOCs [27]. Nevertheless, these processes are not fully understood yet, and the experts are far from having a clear picture linking specific biological pathways to lung cancer, and VOCs profiles.
At this point it should be clear that different pathologies can alter the typologies and concentrations of VOCs in the exhaled breath in different ways. Once properly collected and analyzed, VOCs can therefore function as biomarkers for the monitoring of the healthy state of a patient. It is important to note, as it has been clearly highlighted in a study performed by Wang *et al.* in 2018 [29], that the presence of comorbidities (generally referred to as benign pulmonary diseases in the article) significantly interferes with the VOCs profile of the subject, affecting a possible lung cancer diagnosis; hence, EBA hold a greater potential as a screening tool rather than a diagnostic one, especially for patients with concurring pathologies.

So far, no unique compound has been found to be present only in the exhaled breath of lung cancer patients; a device to be used for screening purposes should instead consider a combination of VOCs in order to retrieve a meaningful signal for the monitoring of the subject's health.
As for which combination of biomarkers could be considered more significant, experts are still debating. A work performed in 2019 by Marzorati *et al.* [30] analyzed 13 studies, from the early 2000s to 2016, that used EBA for lung cancer diagnosis, and reported a total of over a hundred of VOCs found as significant for the discrimination between lung cancer patients and healthy controls; in another work published in 2020, Gerardo Velez and Harvey Pass [31]

Table 2.2: *Brief summary of some amongst the most recurring lung cancer VOCs biomarkers found in literature, divided by class.*

Class	Compounds
Alcohols	Propanol, butanol
Aldehydes	Propanal, butanal, hexanal
Alkanes and alkenes	2-methylpentane, 4-methyloctane, pentane, hexane, decane, dodecane, isoprene
Aromatic compounds	Benzene, propylbenzene, trimethylbenzene, styrene, toluene
Ketones	2-pentadecanone, acetone, butanone, tridecanone

reviewed 53 studies on LC and VOCs, and found a total of 332 VOCs that could be considered as significant biomarkers for LC, from alkanes to aromatic compounds and aldehydes. A brief summary of some amongst the most recurring lung cancer VOCs biomarkers found in literature is presented in Table 2.2 [25, 27, 30, 31]. The main cause for such a variety of results between different studies, both in terms of VOCs profiles and concentrations has to be attributed to the lack of standard in this field. Inconsistencies can be found in:

- Variances in the populations of different studies: factors such as gender, age, smoking history, presence of comorbidities can change from study to study, but they are all factors that influence exhaled breath composition;
- Variances between sampling and storage procedures; even the type of breath portion sampled (i.e. alveolar air or mixed expiratory breath) can be different. This has huge impact on VOCs profile since alveolar air contains mainly endogenous compounds whereas mixed expiratory breath, including also air coming from the anatomical dead space, may be contaminated by exogenous VOCs;
- Variances in data preparation: for instance, some studies may normalize data with respect to the concentration in the exhaled breath while other may use the difference in concentration between exhaled and inhaled air;
- Variances in data analysis: for example, different studies may use different statistical tests, or compare a different number of groups.

2.3 Technologies for exhaled breath analysis

Throughout the years, many techniques have been developed to enhance VOCs extraction and analysis. Exhaled breath can be either collected and analyzed immediately or stored into containers to be transported to a detector. The most common VOCs containers are sampling bags made of Tedlar or Mylar. They offer the advantages of being cheap, chemically inert, and can easily interface with other lab and clinical equipment needed for detection. However, these bags are susceptible to leakage, UV degradation, and water condensation; another issue of using a container as a temporary storage for breath samples is related to the substance instability during storage. This problem could be solved by performing a direct analysis of the breath samples as they are acquired.

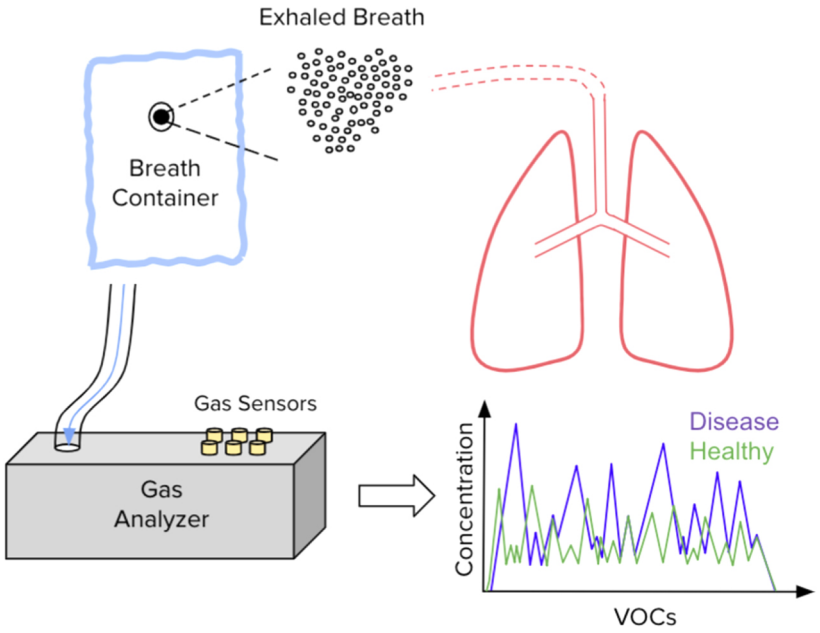

Figure 2.1: *Exhaled breath analysis process: exhaled air is sampled from a patient and collected inside a container; then, it is moved to a gas analyzer whose outcome can be compared with the one of a healthy subject and be used for clinical evaluations of the patient's health state. From [30].*

Once the breath samples are collected, they undergo VOCs detection and profiling, and various techniques (briefly illustrated in subsections from 2.3.1 to 2.3.4) can be adopted. Eventually, these data undergo pre-processing (e.g. data cleaning, baseline correction, dimensionality reduction) and, as the last step, classification techniques (e.g. support vector machine, logisitc regression, pattern recognition) to discriminate between healthy and pathological subjects. A schematic representation of the process, from sampling to analysis is presented in Figure 2.1.

2.3.1 Gas chromatography

In Gas Chromatography (GC), the air sample is combined with a carrier gas; it is then forced towards a stationary component, where a reaction occurs, and eventually the different molecules are separated.
This technique is the most common technique adopted in the analysis of exhaled breath samples, due to its ability to detect VOCs concentration levels even in the part-per-billion range. GC is often used together with Mass Spectrometry (MS) [32, 33], a combination that allows to obtain precise information, both qualitative and quantitative, about the compounds present in the air sample being analyzed.
Nonetheless, it has some serious limits for an application in a clinical setting for a large-scale population screening. This kind of analysis requires expensive technology and must be performed in a laboratory, excluding the possibility of real-time applications. Moreover, it is complex, which leads to the necessity of trained personnel for both usage and results interpretation.

2.3.2 Mass spectrometry

Mass spectrometry works in vacuum. The sample is ionized (for example by bombarding it with a beam of electrons) causing the breakage of the compounds into their constituent ions, which are then separated according to their mass-to-charge ratio by means of an electric or magnetic field. The main principle behind this technique is that ions with the same mass-to-charge ratio will undergo the same deflection, allowing a differentiation between each of them. MS has the advantages of high time resolution and simple sample pre-preparation [34]. Like GC, MS can be used in combination with other techniques and some of them have been employed in EBA, like Proton Tranfer Reaction (PTR) mass spectroscopy [35, 36], which exploits H_3O^+ ions to perform non-dissociative proton transfer and Secondary Electron-Spray Ionization (SESI) mass spectroscopy [37, 38], which ionizes the sample with a nano-electrospray.

2.3.3 Ion-mobility spectrometry

Ion-Mobility Spectrometry (IMS) is based on a 550 MBq ^{63}Ni β-radiation ionising source, which breaks down compounds of the exhaled breath into ions. These ions travel down a chamber at different speeds according to their size, mass and geometry until they hit a Faraday plate at the end of the chamber. Each ion hitting the plate generates an electrical signal which, combined with the signals generated by the other ions, produces a spectrum which is a fingerprint of the exhaled breath [25].
This technique has been exploited alone in some studies like the one carried out by Westhoff *et al.* in 2009 [39] but also in conjunction with time-of-flight MS, providing two-dimensional spectra, thus increasing the information content. Some works such as the one pubblished in 2010 by Reynolds *et al.* [40] have investigated VOCs detection with this complex technique, but a lung cancer specific research seems to still be missing in literature.

2.3.4 Electronic noses

In the last few years, technological advances made possible the development of small, portable array-type devices for the detection and identification of chemicals in gaseous samples on a real-time basis. These devices are called electronic noses, or *e-noses*. They integrate gas sensors and electronic components designed to respond to the mix of compounds in the sample, rather than identify individual compounds like the techniques presented up to this point (i.e. GC, MS and IMS).
The name comes from the fact that their functioning mechanism is similar to the one of the human olfactory system. Our brain is able to identify odours by combining signals generated by the interaction between chemicals present in the air and specific receptors inside the nasal cavity. In an analogous way, these devices exploits arrays of sensors that react with VOCs in exhaled breath. This interaction induces a change in each sensor's property (e.g. conductivity, color or oscillation of a crystal) according to its working principle. Electrical signals produced by each sensor are then combined to generate a composite pattern usually referred to as *breathprint*.
Breathprints are generally complex signals of difficult interpretation; for this reason, they are typically analyzed with some kind of pattern recognition or artificial intelligence algorithm.

Electronic noses differ in many aspects [41]:

- Air sampling technique: every system needs a close environment at the moment of sampling and measurement, to avoid any source of contamination; some e-noses require

a holding canister while others use a balloon;

- Methodological principle: older e-noses measured individual VOCs contrasted by other; modern e-noses exploits pattern recognition in combination with artificial intelligence algorithms and hence need proper training, validation and test sets to be calibrated and optimized;
- Sensor's working principle: e-noses can be built around sensors that exploit different technologies and techniques; the main ones will now be presented.

Colorimetric sensors

Colorimetric devices work with sensors constituted by chemically responsive dyes which, when interacting with some chemicals, change their color. These dyes can be adapted based on the targeted VOC, so that it is possible to build arrays of colorimetric sensors to analyze a broad range of compounds.
The typical setup for EBA with colorimetric sensors requires the sample to pass over the sensors, so that the dyes react and change their color. An image of the array is taken both before and after the exposure, and the entity of the color change is processed to determine the exhaled breath VOCs content.
In literature studies like the ones published by Mazzone *et al.* [42] for characterization of lung cancer or by Zhong *et al.* [43] for LC screening employ this technique. The main advantage of using colorimetric sensors for exhaled breath analysis is the fact that they do not show temperature and humidity dependency [44], which eliminates the necessity to perform water vapor removal from the breath samples.

Quartz microbalance sensors

Quartz microbalance sensors are constituted by quartz crystals coated with varied metalloporphyrins, to which VOCs absorb, changing the mass of the sensors and thus their oscillation frequency [45]. These sensors changes are recorded, and information about the sample chemical content can be inferred.
Some studies on lung cancer identification employing this technique have been published by Di Natale *et al.* [46] and D'Amico *et al.* [47].

Polymeric gas sensors

These sensors exploit changes in electrical properties (variations of resistance and/or capacitance) caused by the absorption of specific VOCs onto their surface. They reach high sensitivities and short response time, but their main advantage, especially if compared to metal oxide sensors, is the ability to ensure these performances at room temperature.
In literature there are some studies relying in this technology for lung cancer applications, like the works of Tirzite *et al.* [48] and Machado *et al.* [49]; both these studies used a popular electronic nose based on conductive polymer gas sensors, the Cyranose 320.

Metal oxide sensors

Metal oxide sensors are composed of a ceramic support tube coated with some oxide material (e.g. SnO_2, ZnO_2). Like conductive polymer sensors, the interaction between the compounds and the surface causes a change in the conductivity of the sensor. They are characterized by high sensitivity and short recovery time, but they operate at high temperatures (somewhere between 200 °C and 450 °C); moreover, the sensitivity can be highly influenced by

the oxide chosen, surface modification (e.g the introduction of noble metal particles, which are high-effective oxidation catalysts that enhance the reactions occurring at surface level), temperature and humidity conditions [50].
The most common electronic nose based on this technology is the Aeonose, which has been used in some works on lung cancer screening such as the study published in 2018 by van de Goor *et al.* [51].

Gold nanoparticle sensors

These sensors are constituted by gold nanoparticles coated with different compounds. When exposed to a breath sample the sensors undergo a reversible change in resistance. In comparison to other types of sensors, gold nanoparticle sensors do not show a humidity dependency, even when exposed to a high humidity environment [52].
Peng *et al.* [52] developed an e-nose with 14 gold nanoparticle electrodes overlaid with a mixture of compounds, and analyzed their response using principal component and cluster analysis.

All the studies presented up to now exploited a variety of instruments, sampling techniques, and different statistical analyses. They have succeeded in the discrimination between lung cancer patients and healthy subjects in the control group; nevertheless, no combination of the instruments, methodologies or statistical analysis has yet been able to reliably perform a prediction on which patients at risk are likely to develop lung cancer. Surely, work has still to be done in the search for the optimal set of instruments and techniques, and further studies and validations on analysis methodologies will help experts advance in this direction. With these limitations, thanks to its simplicity and low cost EBA holds a promising role as a new screening and diagnostic technique in lung cancer.

2.4 Molecularly imprinted polymers

MIPs are synthetic receptors for a target molecule. They have been developed with the intention to mimic the molecular recognition process present in natural systems, i.e. the antibody-antigen mechanism.
Compared to their biological counterpart, MIPs offer comparable specificity and selectivity without the rigid constraint required by natural receptors, that can work and be stored only within the human body temperature range. They have also higher physical robustness and strength [53]. Moreover, their production costs are lower, and their application range is wider, given they can be produced for almost any target molecule (in contrasts with the biological systems where the target must match an available antibody). On the other hand, one of the greatest disadvantages of this technology is the occurrence of non-specific bindings to the imprinted material, due to the absorbent nature of the polymer itself and nonhomogeneous binding sites; another problematic aspect is the need for the removal of the target molecule from the binding site, since any unextracted target interferes with subsequent sensing applications [54].

2.4.1 Production methods

Molecular imprinting of polymers is a process where functional and cross-linking monomers are co-polymerized in the presence of the target molecule (called *imprint molecule*), which provides the molecular template. In the first phase, the functional monomers form a complex

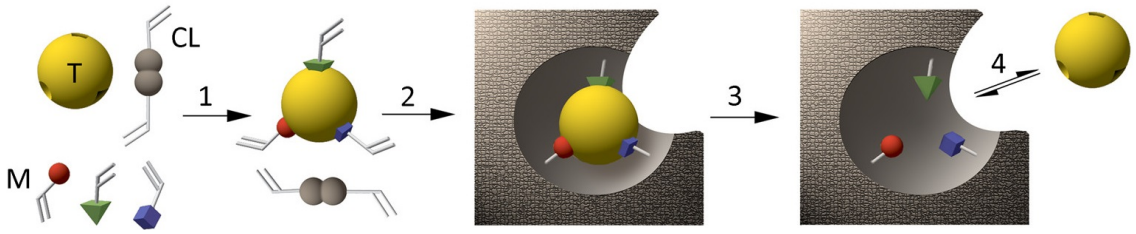

Figure 2.2: *Molecular imprinting phases. Initially, the template molecule (T) and functional monomers (M) bind to form a single complex (1). This step is followed by a polymerization process (2) in presence of a cross-linker (CL). In a final phase (3), the template is removed, leaving the imprinted polymer matrix alone, thus enabling rebinding (4). From [56].*

with the imprint molecule. In the next phase, the polymerization phase, a highly cross-linked polymeric structure is formed, holding the functional groups in position. In the final phase, the imprint molecule is removed from the polymer, leaving a macroporous matrix with microcavities exposing specific binding sites complementary in shape, size and chemical functionality to the template analyte. This process provides the polymer with a molecular memory, enabling its capability of rebinding the analyte with a very high specificity [53, 55]. A schematic representation of the different phases is reported in Figure 2.2. There are two different approaches to molecular imprinting, leading to different characteristics of the binding sites according to the interactions between the monomer and the imprint molecule established during the polymerization phase:

- Self-assembling approach [57]: non-covalent forces (e.g. hydrogen bonds, Van der Waals forces, ion or hydrophobic interactions) are established between template and monomer;
- Pre-organized approach [58]: the imprint molecule and the monomers are linked with covalent, reversible bonds.

The self-assembling approach is the most frequently adopted thanks to the simplicity of complex formation and dissociation and the flexibility it offers in terms of range of monomers that can be employed. The covalent imprinting on the other hand offers more stability of the complex during polymerization, providing higher imprinting efficiency. However, to remove the template from the polymer matrix, the covalent bonds should be cleaved [53, 59]. A scheme showing the differences between the two approaches can be seen in Figure 2.3. Despite the advantages and the potential that molecular imprintig process holds, some drawbacks have to be illustrated. First of all, the design of a new MIP is often a time consuming work that requires a lot of trial-and-error in each aspect of the process, from the synthesis to the testing phase. Another crucial aspect is the affinity with water. More often than not, especially in the biomedical field (where many biomolecules are insoluble or inactivated in organic solvents) the imprinting capability of MIPs in water solutions is crucial; unfortunately, water molecules compete with the template, weakening or even destroying non-covalent interactions between the template and the monomers. Possible solutions found in literature to face this problem are the introduction of cyclodestrines to control electrostatic interactions between template and monomer from water interferences [61] or the introduction of hydrophilic properties to the polymer by exploiting hydrophilic co-monomers [62].

2.4.2 Applications

Molecularly imprinted polymers can be employed in a variety of contexts. For non-sensing applications they are used in targeted drug delivery, chromatography (i.e. *molecularly im-*

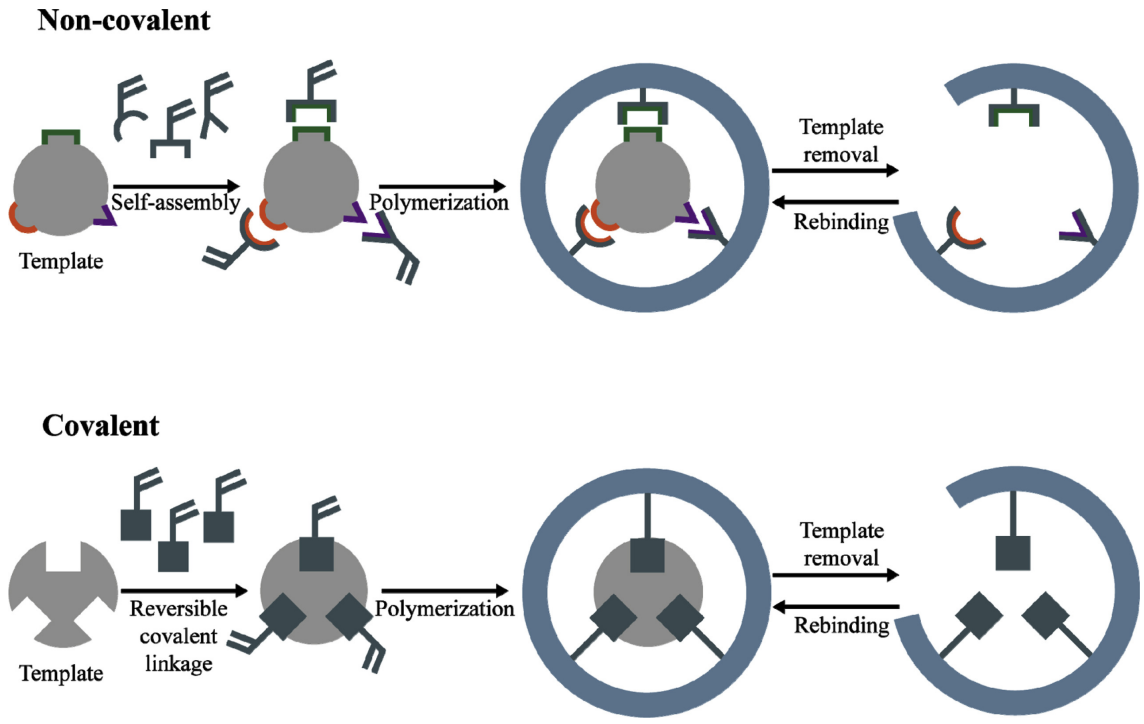

Figure 2.3: *Schematic representation of the self-assembling and pre-organized approaches in MIPs preparation. Differences can be found both in the template-monomers complex formation and in the extraction of the template from the polymer matrix (solvent extraction for non-covalent approach, chemical cleavage for covalent approach). From [60].*

printed chromatography), solid phase extraction procedures (where MIPs can be exploited to selectively extract target analytes from compelx matrices), industrial safety and environmental analyses. In the context of sensing applications, MIPs have found success in the detection of biomarkers (e.g. in substitution of natural-receptor-based tests such as enzyme-linked immunosorbent assay), drugs (e.g. cocaine, glucose, bronchodilators, creatinine), pesticides (e.g. dimethoate, chlorpyrifos, pyrethroid insecticides), food adulterants (e.g. histamine, which at sufficient concentrations is known to cause allergy-like food poisoning).

As for this thesis, the key application for the molecular imprinting technology is gas sensing. In this context, MIPs have been used to build chemosensors able to react with VOCs found in the exhaled breath of lung cancer subjects. A more detailed description of molecularly imprinted polymers used as sensors is presented in section 2.5.

2.5 MIP-based sensors

According to the International Union of Pure and Applied Chemistry (IUPAC) [63], a chemical sensor is:

> A device that transforms chemical information, ranging from the concentration of a specific sample component to total composition analysis, into an analytically useful signal. The chemical information, mentioned above, may originate from a chemical reaction of the analyte or from a physical property of the system investigated.

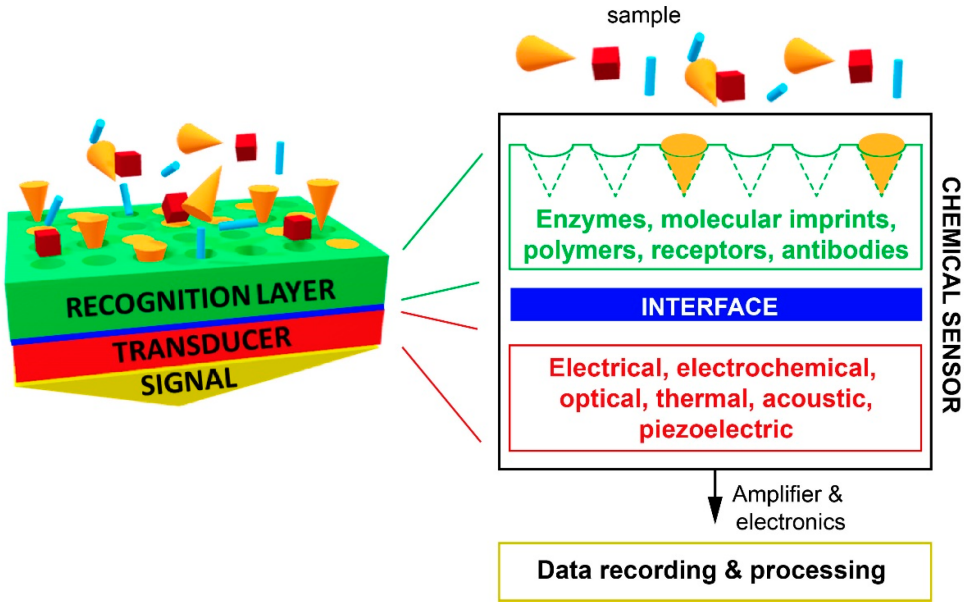

Figure 2.4: *Close inspection of the structure of a chemical sensor. The outer part, exposed to the environment, is the layer in which the recognition elements can be found. This layer interfaces with a transducer, which is able to convert changes in the properties of the recognition elements into a readable signal. From [64].*

Chemical sensors (also referred to as *chemosensors* or *biosensors*) consist of two main elements put in close contact, as it is displayed in Figure 2.4: a recognition element (or *receptor*) and a chemo-physical transducer. The receptor is responsible for the identification of a target analyte, and transforms the binding event into a change of its chemo-physical properties; in the case of MIP-based sensors, the recognition elements is constituted by the imprinted polymer. The transducer is then able to transform these changes into a useful analytical signal that can be read by electronic circuits and further analyzed. According to the transduction process, which can exploit several physical phenomena, such as electrochemical reactions, optical or thermal changes, and mass variations, it is possible to differentiate between different types of chemosensors (the following classification is not intended to be exhaustive nor universal, and is based upon the works performed by BelBruno [54] and Leibl *et al.* [64]).

2.5.1 Electrochemical sensors

In these sensors, the recognition layer is coupled to an electrochemical transducer; depending on the phenomenon exploited for the transduction of the binding event, we can have different subcategories of electrochemical sensors.

Potentiometric sensors

Potentiometric sensors are a low-cost technology that works ideally in absence of current flow and measures the voltage potential difference between a working and a reference electrode. MIPs-based potentiometric sensors are quite popular; they are usually based on (meth)acrylate-MIPs, which ensure low conductivity, hydrophobicity and high selectivity.

Amperometric sensors

Amperometric sensors are widely employed too, and they measure the variations in current flow between the sensor and a reference electrode as a time-dependant, known potential is applied. Due to the lack of physical contact between the analyte and the transducer, the electron transfer (i.e. the current flow) has to be mediated by the sensing element, and conductive MIPs fits this role perfectly. To increase conductivity and obtain a better signal, graphite powder and nanoparticles can be included in the polymer matrices.

Conductometric sensors

Conductometric sensors are based on time-dependent variations in the conductivity of the sensing element triggered by the binding event. Depending on the sensing principle, they can be further classified into two major categories:

- Capacitive sensors: they measure the change in capacitance between two electrodes separated by a dielectric MIP layer (the insulation condition can be easily achieved with (meth)acrylic MIPs). Such variation can be due to a change in the dielectric constant ϵ_r of the material or a change of the geometry.
- Resistive sensors: they measure the change in resistance. Given the fact that resistance depends on the material resistivity ρ and its geometry, a variation can be caused by a change of the resistivity or of the sensor geometry. Differently from the capacitive ones, there is no need to have a sandwich-like structure with multiple layers: only a single electrode layer is needed (in the classic working-reference electrode configuration or in a more complex solution with interdigitated electrodes), with a conductive MIP filling the space in between electrodes. The polymer can be polymerized directly on the electrodes surface or deposited by drop-casting or spin-coating. Conductivity can be given or enhanced by the addition of gold nanoparticles or carbon nanotubes to the polymer.

2.5.2 Optical sensors

These sensors exploit phenomena as fluorescence, chemiluminescence, or colorimetric changes induced by the binding of a target analyte with the imprinted polymer to convert the recognition event into a light signal that can be easily interpreted.
The signal transduction can occur due to inherent optical activity of the target analyte or thanks to the incorporation of a fluorophore or a chromophore into the polymer matrix, which enhance fluorescent activity.
Some methods used for the readout of optical MIP sensors are fluorescence, Surface-Enhanced Raman Scattering (SERS), Surface Plasmon Resonance (SPR), reflectometric and colorimetric interference.

2.5.3 Mass-Sensitive sensors

Within this category fall all the sensors that, due to a mass change, lead to a measurable frequency response. The physical principle at the basis of mass-sensitive sensors is the piezoelectric effect discovered in 1880 by Pierre and Jacques Curie.
Amongst the most common mass-sensitive sensors there are quartz crystal microbalance sensors. The binding of the target analyte with the MIP is followed by a decrease of the oscillation frequency of a piezoelectric crystal (caused by a variation in mass) proportional to the square of the fundamental resonance frequency mode. Once this change is detected,

it can be used for quantitative readouts according to the Sauerbrey equation, which relates the Δf to the Δm.

2.5.4 Characteristics of interest

Regardless of the type of MIP sensor considered, there are some fundamental characteristics that have to be taken into account in the context of the specific application. These parameters are:

- Binding capacity: it is the ratio between the concentration of the target molecule absorbed by the polymer from a solution and the initial concentration of the solution, expressed as a percentage;
- Imprinting factor: it is computed as the ratio between the binding capacity of the imprinted polymer and the binding capacity of the same, non-imprinted polymer;
- Response time: it is the time required by the sensor to reach $(1 - \frac{1}{e}) \approx 63.2\%$ of the final signal, taking as a starting point the onset of the stimulus.

Chapter 3

Materials and Methods

This chapter covers the main methodological aspects behind the development of the device, alongside some necessary theoretical background.

3.1 Sensors

In the development of a device for the analysis of gaseous samples, a key role is played by the sensing elements, which enable the recognition of specific, target analytes present in the sample and provide a readable signal. The development of the chemosensors, both in terms of the recognition layer (i.e. the molecularly imprinted polymer) and its interface with the transducer, an interdigitated electrode fabricated and commercialized by MicruX Technologies (see subsection 3.1.4), has been carried out by the team of Professor Francesco Cellesi and Francesco Bosatelli at Politecnico di Milano's Applied Physical Chemistry Lab (Department of Chemistry, Materials and Chemical Engineering 'Giulio Natta').

3.1.1 Target analytes

In the context of this thesis, the focus has been put on three different target analytes, and their detection has been made possible by the realization of three respective MIPs.

Toluene

Toluene ($C_6H_5CH_3$), also know as methylbenzene, is an aromatic hydrocarbon composed of a benzene ring (C_6H_6) having a hydrogen bond substituted with a methyl group (-CH_3). A three dimensional model of the molecule can be seen in Figure 3.1.
Toluene is a colorless liquid with a characteristic aromatic odor used as a solvent (e.g in paints, coating, inks and cleaning agents) or as a chemical intermediate in various industrial applications (e.g. added to gasoline to improve octane ratings).
Toluene is a toxic air pollutant that can be absorbed by individuals exposed to it. Exposure can induce mild, acute symptoms such as fatigue, sleepiness, headaches, and nausea but also more severe, chronic conditions especially at central nervous system level such as nystagmus, impaired speech and hearing. For this reason, the Occupational Safety and Health Administration (OSHA) has fixed an 8-hour time-weighted permissible exposure limit of 200 part-per-million and a recommended limit of 100 part-per-million [65].

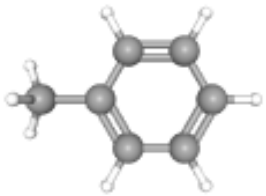

Figure 3.1: *Toluene 3D conformer. From [65].*

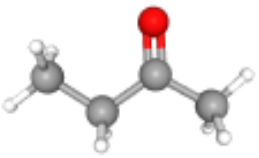

Figure 3.2: *Butanone 3D conformer. From [68].*

Toluene is well metabolized by hepatic cytochrome p450 enzymes and eliminated mainly in the urine, but a portion is exhaled unchanged.
There are several studies that assessed the importance of toluene as a biomarker for lung cancer, but while some of them [32, 36] reported a statistically significant increment in its concentration in the exhaled breath of lung cancer patients with respect to the control group, others [66, 67] found a decrease in concentration probably related to the the overactivation of p450 enzymes in lung cancer. These contradictory results show that there is still a lot of work to be done in the comprehension of lung cancer VOCs metabolism. Regardless of the study, concentrations found were in the order of 10^0 to 10^2 part-per-billion.

Butanone

Butanone ($CH_3COCH_2CH_3$), also know as methyl ethyl ketone, is a ketone composed of a carbonyl group (-CO) attached to a methyl (-CH_3) and ethyl (-CH_2CH_3) group. A three dimensional model of the molecule can be seen in Figure 3.2.
Butanone is a colorless liquid that can be synthesized, but is also present in nature (in some trees, fruits and vegetables). It is primarily used in paints and other coatings; it is also used in glues and as a cleaning agent.
Short-term inhalation exposure to butanone causes irritation to the eyes, nose, and throat. Limited information is available on the chronic (long-term) effects. The OSHA has fixed an 8-hour time-weighted permissible exposure limit of 200 part-per-million [68].

Ketones are readily absorbed through the intact skin. They rapidly transfer to the blood and thence to other tissues. Methyl ethyl ketone and its metabolites are primarily excreted

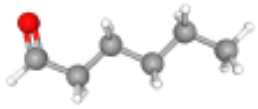

Figure 3.3: *Hexanal 3D conformer. From [71].*

via lungs and kidneys, but the fractional elimination of the unchanged molecule depends on metabolic activity and exposure; for the exhaled air it is generally around 10% of the absorbed dose [69].
Different studies [36, 66, 67, 70] identified butanone (in concentrations in the order of 10^1 part-per-billion) as a VOC that could be possibly considered as a lung cancer biomarker. Nevertheless, as for the toluene, there is still a lack of knowledge on its behaviour in lung cancer subject with respect to healthy population.

Hexanal

Hexanal (C_6H_12O), also know as hexaldehyde, is a saturated fatty aldehyde similar to hexane, in which one of the terminal methyl groups (-CH_3) has been mono-oxygenated. A three dimensional model of the molecule can be seen in Figure 3.3.
Hexaldehyde appears as a colorless liquid and it is employed in the chemical industry for the syntesis of dyes and insecticides; it is widely used as a fruit flavor in chewing gums, hard candy, beverages and, when highly diluted, in perfumery.
Exposure to hexanal can induce mild symptoms such as discomfort in the eyes and nose, and headache; for concentrations of 10 part-per-million also nasal obstructions were observed. Overall, no severe conditions were registered on humans, mainly due to the lack of experiments performed.

Hexanal is known to be generated through peroxidation of unsaturated fatty acids. Elevated concentrations in the exhaled breath of lung cancer subject may, therefore, be attributed to the enhanced oxidative activity of the tumor tissue, but may as well derive from oxidative stress enhanced by the local inflammatory processes caused by the interactions between the organism and the tumor [72]. These explanations have found experimental feedbacks, in particular in a study performed by Fuchs *et al.* [73] where hexanal concentrations in exhaled breath (albeit very low, less than 1 part-per-billion) were significantly higher in lung cancer patients than in smokers and healthy control subjects.
Therefore, developing sensors with the ability to detect hexanal is certainly an important step in the realization of a lung cancer screening tool.

3.1.2 MIP-based sensors: preparation procedure

The work of this thesis has been focused on the realization of both capacitive and resistive MIPs for each one of the three analytes. The main steps for the preparation of the imprinted polymers and their deposition onto the electrodes will now be presented.

1. **Cleaning**: in order to remove any external and undesired substance, all the electrodes (both new and used) undergo a cleaning procedure. The procedure for used electrodes is complex and depends on the MIP deposited onto it, so it will not be covered here. For new electrodes, each cycle consist in 5 minutes of immersion in de-ionized water followed by 5 minutes in ethanol. This step is repeated three times, followed by a 5 minutes immersion in acetone. When electrodes dry out, they are put for 30 minutes in an ozonizer.

2. **Functionalization**: in this phase, the cleaned electrodes are put in a 5 millimolar solution of Bis(2-methacrylol)OxyethylDiSulphide (BODS) in ethanol. They are kept in a dark environment for one night. The BODS has the ability to strongly bind with the gold surface of the electrodes, functioning as an anchor point for the polymer that will be deposited: this procedure provides the interface between the recognition layer and the transducer.

3. **Thin-film deposition**: specific quantities (illustrated in Table 3.1) of cross-linker, functional monomer, initiator and target analyte are put together in a solution. Then, for capacitive MIPs, diacetylene (in a 1:4 ratio with the total volume of cross-linker and monomer) is added to the solution in order to strengthen variations of dielectric properties, whereas for resistive MIPs 0.2 mg/mL of carbon nanotubes are added to make the polymer conductive.
   The deposition of the polymeric solution can be done by:

   - Drop-coating: used for both capacitive and resistive MIPs. It requires the deposition of a single drop of solution onto the sensing area of the electrode. Before deposition, the polymeric mixture is eventually put in a solution at 20% with dichloromethane. In this way by depositing a very small quantity of solution (15 μL), the 80% will evaporate due to the low evaporation temperature of dichloromethane and the film that forms on the electrode has a thickness lower than it would be possible to achieve with a drop of the polymeric solution only;
   - Spin-coating: used only for capacitive MIPs. A certain quantity of solution is deposited onto the active area of the electrode, then the sensor is put onto a spin-coater run at 800 rpm for 10 seconds and at 2000 rpm for other 10 seconds. This method, with respect to the drop-coating, ensures a more uniform deposition and controlled thickness.

4. **Polymerization**: the deposited material passes from liquid to solid in a photopolymerization process, which requires the sensor to be exposed for 5 minutes, in absence of oxygen, to UV light ($\lambda = 365\ nm$).

5. **Template removal**: eventually, the imprint molecule is removed from the polymer through evaporation or by means of a solvent (acetone). This last step enables further rebinding of the target molecule with the polymer. After a 24-hours stabilization period the sensors will be ready to be used.

3.1.3 MIP-based sensors: characterization

The choice of the proper functional monomer for each one of the three MIPs has been investigated by Professor Francesco Cellesi and Francesco Bosatelli by means of UV spectroscopy. In particular, they analyzed the absorbance capabilities of the MIPs originated from 4 different functional monomers:

Table 3.1: *Composition of the initial polymeric solution for the recognition of each analyte. The numbers inside the brackets represent the number of equivalent used for each substance inside the solution.*

Cross-linker	Functional monomer	Initiator	Imprint molecule
EGDMA[1](40)	MAA[2] (10)	AIBN[3] (1)	Toluene (4)
EGDMA (5)	BzMA[4] (10)	AIBN (1)	Butanone (4)
EGDMA (5)	ChMA[5] (10)	AIBN (1)	Hexanal (4)

[1] Ethylene glycol dimethacrylate.
[2] Methacrylic acid.
[3] Azobisisobutyronitrile.
[4] Benzyl methacrylate.
[5] Cyclohexyl methacrylate.

- MethAcrylic Acid (MAA)
- Butyl MethAcrylate (BuMA)
- Benzyl MethAcrylate (BzMA)
- Cyclohexyl MethAcrylate (ChMA)

The results of their analysis can be seen in Figure 3.4. Each graph represents the ratio between the mass of the absorbed solvent and the mass of the polymer. This ratio has been computed for each MIP and its respective Non-Imprinted Polymer (NIP), synthesized from each one of the four functional monomers under examination. From these graphs the value of the imprinting factor can be inferred, by dividing the MIP mass ratio for its corresponding NIP mass ratio. The best functional monomer is the one that maximizes the imprinting factor, hence for toluene MAA has been chosen, for butanone BzMA and for hexanal ChMA.

3.1.4 Interdigitated electrodes

The imprinted polymers have been deposited onto a particular type of electrodes, called IDE. For this particular application, both the ED-IDE1-Au and the ED-IDE3-Au (Figure 3.5) produced by MicruX Technologies [74] have been employed. They consist of two thin-layer gold strips, i.e. the working electrodes WE1 and WE2 deposited on a glass substrate; each working electrode has a pad on one end to interface with the acquisition system, and a comb of sensing microelectrodes on the other end, disposed in a planar, interdigitated circular pattern. All the surface, except from the pads and the circular sensing area, is covered with an insulating layer made of EPON SU8 resin. Table 3.2 summarizes the main features and differences between these IDE. According to the type of MIP (dielectric or conductive) deposited onto the sensing area of the IDE, it is possible to obtain a chemosensor to be used for capacitive or resistive measurements.
The main advantage of using IDE versus a single electrode configuration is that all the pairs are in parallel.

- For capacitive sensors, the total capacitance of the system is incremented by a theoretical factor of $n - 1$ (n being the total number of parallel plates), which aids the measurement phase: using the frequency-based method described in subsection 3.2.2, the lower the capacitance to be measured, the higher the frequency to be detected;

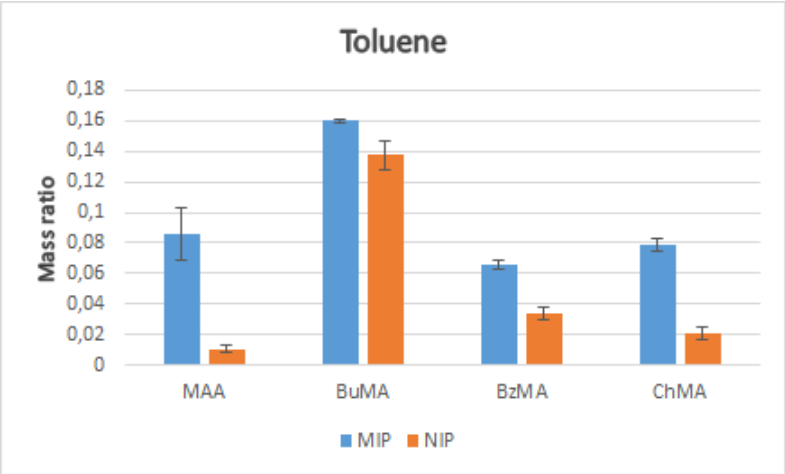

(a) *Mass ratio analysis to investigate the best functional monomer for a toluene-imprinted polymer.*

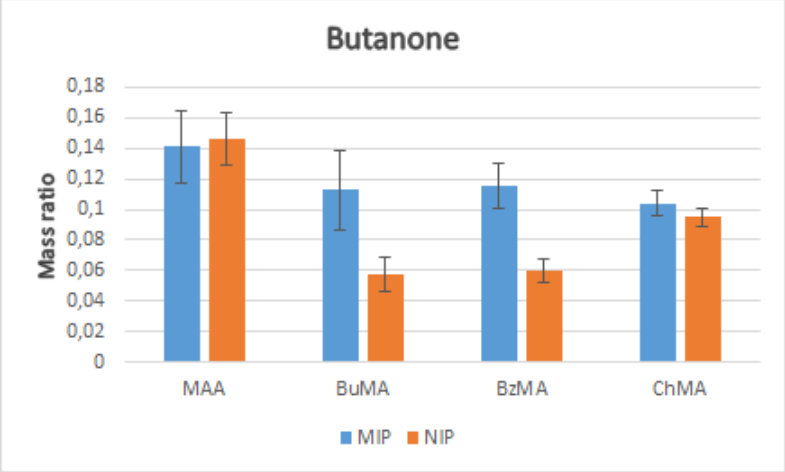

(b) *Mass ratio analysis to investigate the best functional monomer for a butanone-imprinted polymer.*

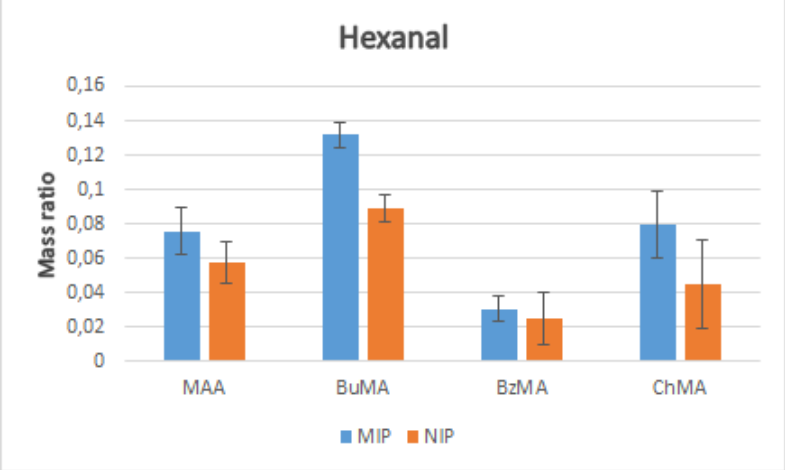

(c) *Mass ratio analysis to investigate the best functional monomer for a hexanal-imprinted polymer.*

Figure 3.4: *Characterization of the three different MIPs. These graphs have been provided by Francesco Bosatelli.*

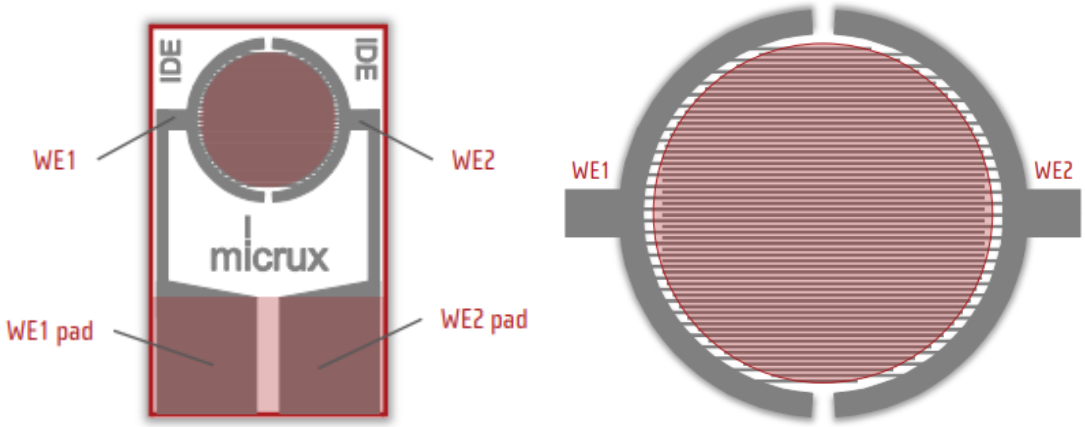

(a) *Electrode.* **(b)** *Zoom on the sensing area.*

Figure 3.5: *Interdigitated electrodes by MicruX Technologies. From [74].*

Table 3.2: *Summary of the features of the ED-IDE1-Au and ED-IDE3-Au interdigitated electrodes produced by MicruX Technologies.*

	ED-IDE1-Au	**ED-IDE3-Au**
Dimensions	10x6x0.75 mm	10x6x0.75 mm
Substrate	Glass	Glass
Insulating layer	EPON SU8 resin	EPON SU8 resin
Electrochemical cell	3.5 mm $\varnothing$	3.5 mm $\varnothing$
Electrodes material	Gold	Gold
Electrodes thickness	50/150 nm	50/150 nm
Microelectrode width	10 μm	5 μm
Microelectrode gap	10 μm	5 μm
Number of fingers	90 pairs	180 pairs

hence, a higher capacitance helps relaxing the conditions around the operational frequencies.

- For resistive sensors, the total resistance of the system is reduced by a theoretical factor of $1/n^2$. The first reduction term comes from the assumption that each pair forms a resistor shorter by a factor of $1/n$ with respect to the 'entire' single electrode resistor, hence each pair has a resistance which is $1/n$ of the initial one; the second $1/n$ reduction term is due to the parallel configuration of the n-assumed-equal resistors. Also in this scenario the measurement phase is made easier: in fact, being the resistance lower, the tensions generated will be lower too (and the employed instrumentation imposes some operative constraints on tensions, as explained in subsection 3.2.3).

IDE support and interface

To hold the electrodes firmly in position, and at the same time guarantee an effective electrical interconnection with the measurement system, two different solutions have been implemented.

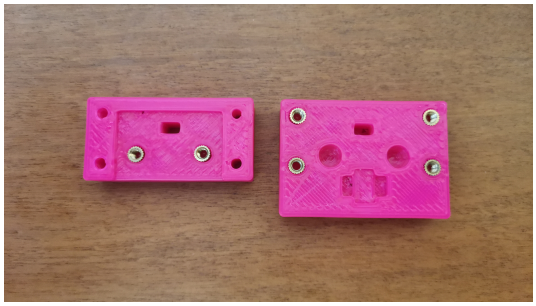

(a) *On the left: top part. On the right: bottom part.*

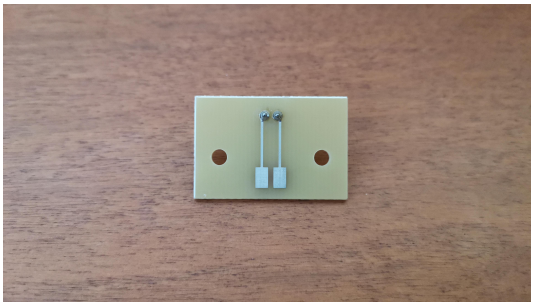

(b) *PCB.*

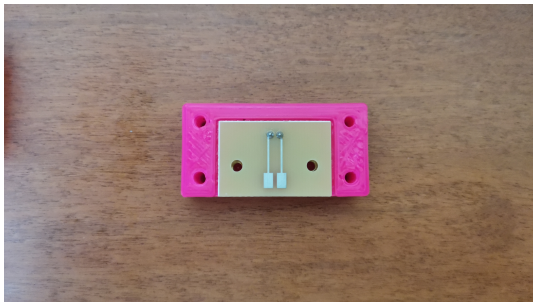

(c) *Top part with PCB mounted (not screwed).*

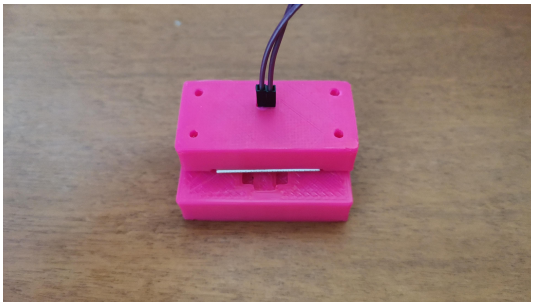

(d) *Top and bottom part mounted (not screwed).*

Figure 3.6: *Custom 3D printed supportive case designed with Fusion 360. The overall dimensions of the case are 50x35x24 mm.*

The first one is the custom 3D printed supportive case that can be seen in Figure 3.6. It has been designed using Fusion 360, an extremely versatile software distributed by Autodesk that includes within the same environment CAD, CAM, CAE and PCB design tools. The case is made of Polylactic Acid (PLA) and consists in a bottom part, which has a cavity to harbor the electrode, and a top part to which the second solution, i.e. the interfacing PCB, can be secured; the two parts are then screwed together to ensure electrical contact between the pads of the IDE and the pads of the PCB. The whole chamber is then connected to the measurement system through a couple of cables, visible in Figure 3.6d, attached to the two pins of the PCB that have been made accessible from the outside thanks to a hole in the top part. The PCB design has been kindly provided by Davide Marzorati. Both the schematic and the board, produced with the Autodesk software EAGLE, are reported in Figure 3.7.

In reality, these solutions have been realized but never employed. During the experiments performed in laboratory, an analogous setup has been used: the all-in-one platform from MicruX Technologies [75] shown in Figure 3.8, which is more practical and possesses superior build quality. The connection between the chamber and the measurement system is made via a mini-USB cable provided together with the platform.

3.2 Measurement system

As said previously, when the target analyte binds with the recognition layer of the chemosensor, a change in its physical properties produces a variation in its capacitance or resistance value. To monitor and quantify these changes, an external source of excitation is required. Hence, these types of sensors are defined as *active* sensors.

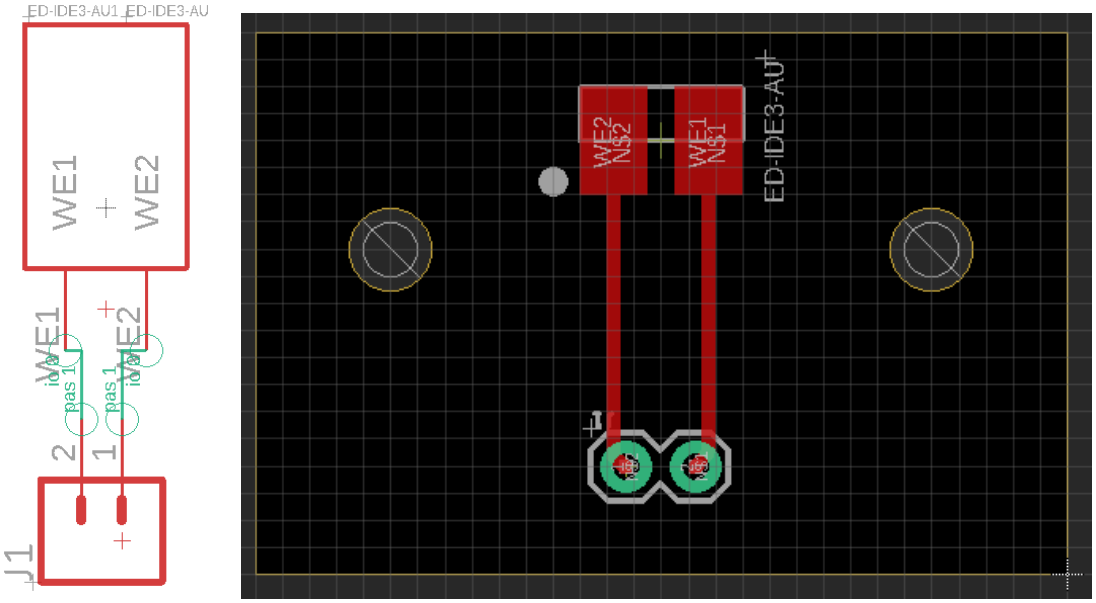

(a) *PCB schematic.* (b) *PCB board.*

Figure 3.7: *PCB design provided by Davide Marzorati and realized with Autodesk EAGLE. The dimensions of the PCB are 20x30 mm, and the two holes needed to secure the PCB to the top of the case have a diameter of 3 mm.*

Figure 3.8: *All-in-one platform from MicruX Technologies. From [75].*

The techniques employed to acquire these signals, alongside their implementation, will be covered in subsections 3.2.2 and 3.2.3, after a brief introduction on the core element of the whole system: the Programmable System on Chip (PSoC) 5LP Prototyping Kit.

3.2.1 PSoC

A microprocessor is a digital integrated circuit containing arithmetic, logic and control units for the execution of a sequence of instructions provided by a program. A microcontroller is

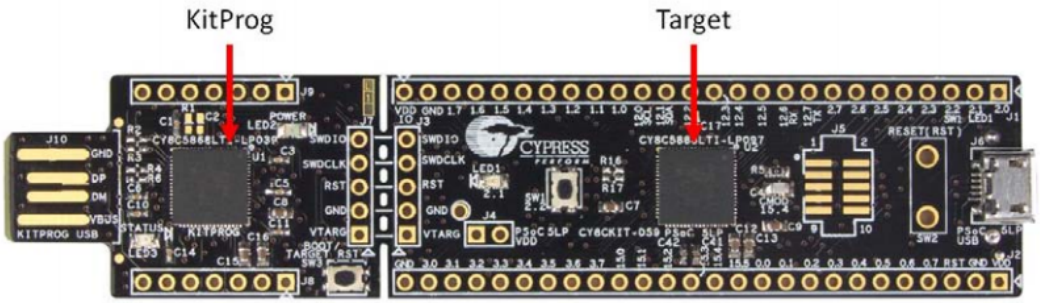

Figure 3.9: *CY8CKIT-059 PSoC 5LP Prototyping Kit by Cypress Semiconductor Corporation. The two components, i.e. the KitProg and the Target device, have been highlighted. From [76].*

a micropocessor with added functionality such as memory (e.g. RAM, flash) and peripherals including communication blocks (e.g. I2C, USB, UART), timing blocks (e.g. timers, counters), analog signal processing blocks (e.g. ADC, DAC, analog comparators). A System on Chip follows the same logic of a microcontroller, but is usually integrated with more advanced peripherals such as GPU, WiFi or Bluetooth modules, or even with co-processors. A Programmable System on Chip offers even more flexibility to the user, combining programmable and reconfigurable analog and digital peripherals with flexible routing.
For the purpose of this thesis, the CY8CKIT-059 PSoC 5LP Prototyping Kit [76] developed by Cypress Semiconductor Corporation has been chosen. It is based on a 32-bit ARM Cortex-M3 CPU and is composed of two parts: the actual, target device and the Cypress KitProg, which is used to program and debug the target PSoC 5LP device and enables some bridging functionality, such as USB-UART and USB-I2C; the KitProg can also be detached in a final stage to optimize the encumbrance of the chip. The device at issue is depicted in Figure 3.9.
The PSoC 5LP (referred to as just *PSoC* in the following) has been programmed with a firmware designed not only to control the electronic circuitry in charge of the acquisition and processing of the signals generated by the chemosensors, but also to transmit these data via UART to an external PC equipped with the GUI specifically developed for this purpose and presented in section 3.3.
The firmware has been developed inside the IDE dedicated to Cypress PSoC devices: 'PSoC Creator', which allows not only hardware and firmware editing, but is also provided with compiling and debugging tools.

A microcontroller, and hence the PSoC, is not able to directly measure the capacitive or resistive changes of the chemosensor: the basic electrical parameters it can work with are voltage, time, and frequency. The output of the sensor must then be converted to one of these three types of electrical parameters to be digitally acquired. This is the purpose of the so called analog front-end circuits that have been implemented and will now be discussed.

3.2.2 Capacitance readout

Principles

The electrical capacitance (or simply *capacitance*) is defined as:

$$C = \frac{Q}{V} \tag{3.1}$$

It is measured in farad (F), which indicates the amount of electric charge Q stored per unit of electric potential difference V applied to an object.

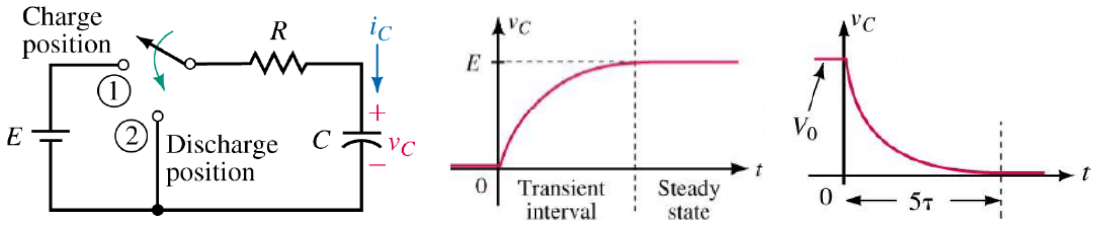

(a) *Simple RC circuit for the charge (switch in position 1) and discharge (switch in position 2) of a capacitor.*

(b) *Capacitor charge process.*

(c) *Capacitor discharge process.*

Figure 3.10: *Figure (a) shows the topology of an RC circuit. Figure (b) displays the behaviour of the capacitor voltage V_C being charged and highlights the transient and steady state phases. Figure (c) instead displays the behaviour of the capacitor voltage V_C being discharged and highlights how the steady state is reached approximately after a period of time equal to 5τ.*

A capacitor is a passive electronic component that, in its simplest version, consists in a pair of parallel conductors (usually called *plates*) separated by vacuum or by a layer of an insulating material called *dielectric*. For an object of this type, its capacitance can be expressed as:

$$C = \epsilon_0 \epsilon_r \frac{A}{d} \tag{3.2}$$

where $\epsilon_0 \approx 8.854 \times 10^{-12}\ F/m$ is the vacuum permittivity, ϵ_r is the permittivity of the dielectric material inserted between the plates, A is the area of each plate and d the distance between them. In this project each sensor is built around an IDE, which in the case of a capacitive MIP-based sensor can be modeled as a parallel plates capacitor with n plates (n being 181, given the IDEs employed have 180 pairs of fingers), whose capacitance can be written as:

$$C = \epsilon_0 \epsilon_r \frac{A}{d}(n-1) \tag{3.3}$$

ϵ_r indeed plays the most important role in this application. As a consequence of the binding with the target analyte, the dielectric properties of the polymer change producing an increment in the total capacitance of the sensor.

A capacitor can be charged or discharged by applying a voltage across its terminals through a series resistor, as it can be seen in the circuit shown in Figure 3.10a. Both these processes can be mathematically described by two equations that show the behaviour of the voltage across the capacitor over time. Being V_0 the initial voltage of the capacitor and E the voltage applied, the charge process (Figure 3.10b) is described by:

$$V_C(t) = E + (V_0 - E)e^{-\frac{t}{\tau}} \tag{3.4}$$

while the discharge process (Figure 3.10c) from an initial voltage V_0 is described by:

$$V_C(t) = V_0\ e^{-\frac{t}{\tau}} \tag{3.5}$$

The parameter τ is also called *time constant* of the circuit and, in this example, is equal to RC. It is measured in seconds and it represents the time it takes for V_C to reach 63.2% of its steady state value in the charge phase, or 36.8% of its starting value in the discharge phase.

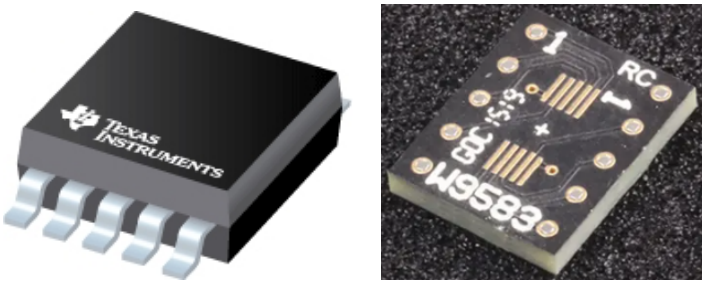

(a) *FDC1004Q 10-pin VSSOP package. From [77].*

(b) *Winslow Adaptics 10-pin female SOP to 10-pin male DIP adapter. From [78].*

Figure 3.11: *The Texas Instruments FDC1004Q capactiance-to-digital converter in Figure (a) has been soldered to the SOP-to-DIP adapter by Winslow Adaptics in Figure (b) to enable its use on a prototyping breadboard.*

Implementation

The developed device is able to perform capacitive measurements in two different ways, one based on a commercial product and the other one relying on PSoC components only.

The first method exploits an external sensor, visible in Figure 3.11: the FDC1004Q 4-channel capacitance-to-digital converter provided by Texas Instruments [77]. It is a low-cost, high-resolution (up to 0.5 fF) instrument that can measure grounded capacitors within a range of ± 15 pF, and can handle a sensor offset up to 100 pF, which can be either internally programmed or an external capacitor. It includes shield drivers for sensor shields, which can reduce electromagnetic interference. It can communicate with the PSoC exploiting the I2C protocol; the code necessary to both configure the sensor and collect data is available on GitHub at the following link: `https://github.com/dado93/PSoC-FDC1004Q` and has been provided by Davide Marzorati. It has to be noted that the PSoC operates at 5 V whereas the FDC1004Q works with tensions of 3.3 V; hence, a voltage regulator [79] and a bi-directional logic level converter [80] have been employed to create a proper interface between the two units.
This solution has been mainly used as a reference to evaluate the performances of the method entirely based on PSoC, which will now be discussed.

The second method relies entirely on the PSoC capabilities, and performs capacitive measurements exploiting the relaxation oscillator circuit visible in Figure 3.12a. An inverting comparator is used to generate a self-oscillatory behaviour. When the output $COMP\_OUT$ of the comparator is logic high (V_{dd}), the capacitor C_{sense} is charged through $R1$; when the voltage across the capacitor, which is the input of the non-inverting pin of the comparator, reaches the upper threshold value

$$V_{TH} = \frac{(R2 + R4)R3}{R2R3 + R3R4 + R2R4} \cdot V_{dd} \tag{3.6}$$

at the input of the inverting pin, the output of the comparator drops to logic low (0 V). Now the opposite process happens: C_{sense} discharges, starting from V_{TH}, until its voltage drops below the lower threshold value

$$V_{TL} = \frac{R3R4}{R2R3 + R3R4 + R2R4} \cdot V_{dd} \tag{3.7}$$

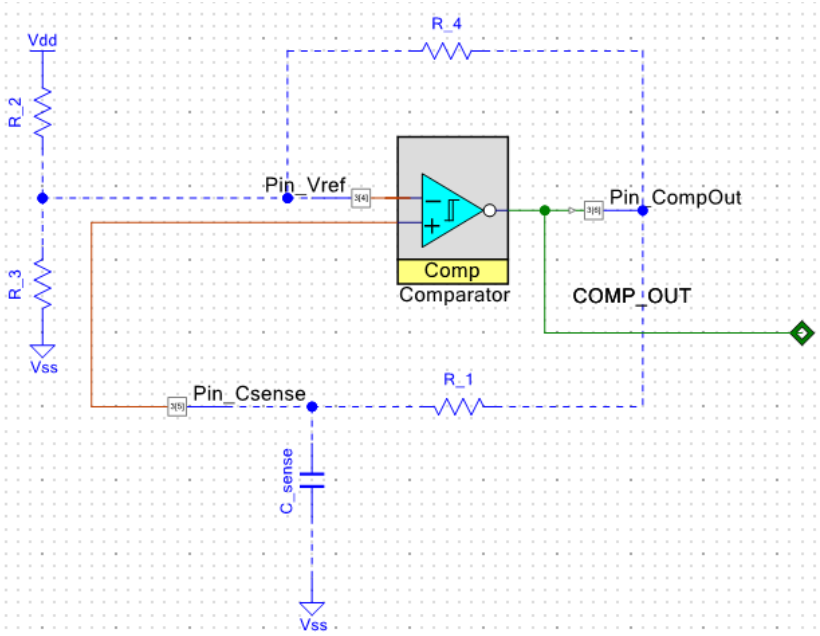

(a) *Relaxation oscillator circuit.*

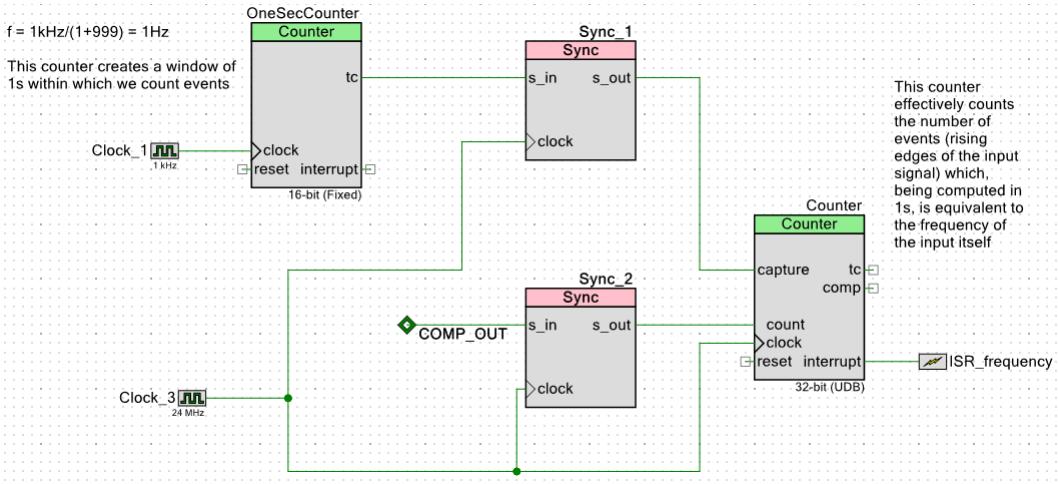

(b) *Frequency computation blocks.*

Figure 3.12: *Circuit and digital blocks involved in the PSoC capacitive measurement method based on a relaxation oscillator.*

Now the voltage at the inverting pin is higher than the voltage at the non-inverting pin, hence the output of the inverting comparator jumps to V_{dd} and the cycle is repeated: a square wave is generated.
The threshold switches from V_{TH} to V_{TL} dynamically depending on the output of the comparator but the individual levels can be set by choosing the desired values for $R2$, $R3$ and $R4$. In this application $R2 = R3 = R4 = 10\ k\Omega$ have been chosen, to guarantee an output square wave with a duty cycle of 50%. Hence, from equation 3.6

$$V_{TH} = \frac{2}{3}\ V_{dd} \tag{3.8}$$

and from from equation 3.7

$$V_{TL} = \frac{1}{3}\ V_{dd} \tag{3.9}$$

The key concept here is that, while the values of the resistors affect the thresholds, the frequency of the square wave depends on the charge-discharge cycle of the capacitor C_{sense}, which in turn is determined by the time constant of the network $\tau = R1C_{sense}$. In particular, being $T1$ (from equation 3.4)

$$T1 = \tau \ln\left(\frac{V_{dd} - V_{TL}}{V_{dd} - V_{TH}}\right) \tag{3.10}$$

the time it takes for C_{sense} to reach V_{TH} from an initial voltage of V_{TL}, and being $T2$ (from equation 3.5)

$$T2 = \tau \ln\left(\frac{V_{TH}}{V_{TL}}\right) \tag{3.11}$$

the time it takes for C_{sense} to return to V_{TL}, it is possible to retrieve the period of the square wave as $T = T1 + T2$. Hence the frequency f can be expressed as:

$$f = \frac{1}{T} = \frac{1}{\tau \ln\left(\frac{V_{TH}}{V_{TL}} \frac{V_{dd}-V_{TL}}{V_{dd}-V_{TH}}\right)} \tag{3.12}$$

By utilizing equation 3.8 and 3.9, equation 3.12 becomes:

$$f = \frac{1}{1.38\ \tau} \tag{3.13}$$

Connecting $COMP\_OUT$ to a series of blocks, as shown in Figure 3.12b, that are able to count the number of rising edges within a predetermined period of time, it is possible to measure the frequency of the generated square wave. Hence, the unknown value of C_{sense} can be easily retrieved from equation 3.13 as:

$$C_{sense} = \frac{1}{1.38\ fR1} \tag{3.14}$$

The value of $R1$ is known and in this application is equal to 1 $M\Omega$. It is also possible to compensate for parasitic capacitances biasing the result by performing a measurement with no capacitor connected and subtracting from equation 3.14 the obtained value.

Firmware workflow

As for the code, it has been given to the user the choice of the measurement method he wants to adopt.

- If the user requests a capacitive measurement that involves the FDC1004Q sensor, at first its registers are set up to continuously acquire data; an automatic calibration procedure has been implemented within the measurement process to find the correct value for the programmable offset and extend the operative range of the instrument. After each measurement the offset is reset to track any possible decrease greater than 15 pF. When the user is done, he can stop the measurement.
- If the user requests a PSoC capacitive measurement, *OneSecCounter* generates a one-second window within which *Counter* counts the number of rising edges of the generated square wave, hence providing a direct measurement of its frequency. Then, equation 3.14 is applied to retrieve the value of the capacitance of the sensor. Again, this process can be stopped in any moment by the user.

The firmware is fully available at `https://github.com/AndreaRescalli/Tesi_Rescalli/tree/main/Thesis/RC-Meter.cydsn` and every step is commented to facilitate its comprehension.

3.2.3 Resistance readout

Principles

The electrical resistance (or simply *resistance*) is a property of an object that quantifies its opposition to the flow of an electric current. In many materials, the current I flowing through them is proportional to the voltage V applied across their extremities, and the term that links these two quantities is the resistance R. This relation is summarized by the global version of the Ohm's law (opposed to the local version which links the current density to the electric field at any given point in the material):

$$V = IR \tag{3.15}$$

Resistance measurement unit is the ohm (Ω), and materials governed by equation 3.15 are defined as *ohmic* materials.
There is another relation that is important to highlight, the Pouillet's law:

$$R = \frac{l}{\sigma A} \tag{3.16}$$

Equation 3.16 refers to an ideal case of a uniform material, with electric field and current density parallel and constant across its entire length; it is here presented with the sole purpose of introducing in a general way the mechanism behind resistance variations in the developed chemosensors.
This equation expresses the dependence of the resistance from the physical properties of the material of which it is made of. In particular, it is directly proportional to the length l, expressed in meters (m), but inversely proportional to the cross-sectional area A, expressed in squared meters (m^2). The remaining term is the conductivity σ, expressed in Siemens per meter (S/m), which is a measure of the material's ability to conduct electric current.
Conductivity indeed plays the most important role in this application. As a consequence of the binding with the target analyte, the imprinted polymer swells. This expansion increases the distance between the carbon nanotubes that have been added to the matrix, disrupting the conducting pathways for the charge carriers [81]. As a consequence, the conductivity of the material decreases and, according to equation 3.16, resistance increases. The mathematical formulations that explain this mechanism are very complicated and not fully consolidated yet; there are some works like the one performed by Vercelli *et al.* [82] who used Mott's theory of variable-range hopping conductivity to retrieve an analytical expression for the variation in conductivity after swelling, but this lies outside the context of this thesis.

Implementation

The resistance of the chemosensor is sensed with a reference resistor method in a four-wire configuration.
A four-wire configuration, shown in Figure 3.13, is a method that reduces measurement errors induced by wire resistances. A known, constant current I_S is sent through the load along one path, whereas the voltage V across R is measured on a different path. This ensures that the value of the unknown resistor, calculated inverting the equation 3.15 accordingly, will not be affected by the voltage drops across wire resistances R_{w1} and R_{w4}, which are bypassed. The current that passes through R can be assumed equal to I_S because the voltage is being sensed by a high input impedance ADC, meaning the current flow on the sensing path is negligible; at the same time, this ensures that across R_{w2} and R_{w3} there is almost no voltage drop. To have an accurate measurement, the current source and the ADC used to measure

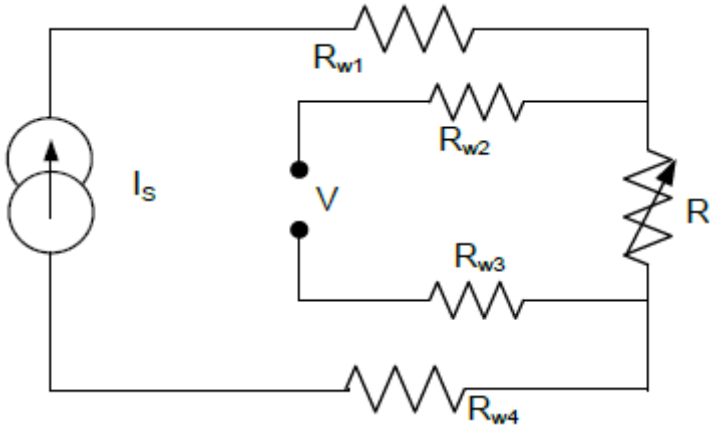

Figure 3.13: *Four-wire configuration for the measurement of a variable resistor R. The source path and the measuring path are clearly separated. From [83].*

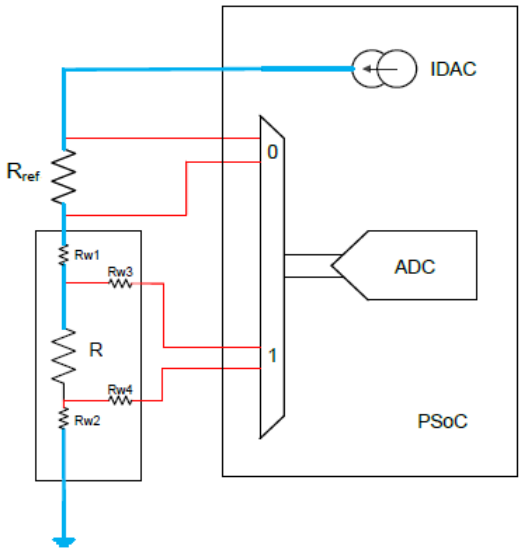

Figure 3.14: *Reference resistor measurement method with a PSoC device. The sensor R and the reference resistor R_{ref} are put in series and the voltage across them is acquired with a four-wire configuration. From [83].*

the voltage should not be affected by offset, gain and non-linearity errors. Given this is not possible in a real instrument, some solutions can be adopted to compensate for these errors. For this purpose, the reference resistor method has been implemented.
As shown in Figure 3.14, this method simply consists in putting a reference resistor R_{ref} in series with the resistance R to be measured. Then, a known current is injected into the circuit with an IDAC and the voltage across both resistors is sensed by an ADC. Considering in first approximation the voltage drop across wire resistances R_{w1} and R_{w2} negligible, the value of R is given by:

$$R = \frac{V_R}{V_{R_{ref}}} \cdot R_{ref} \tag{3.17}$$

Where V_R is the voltage across R and $V_{R_{ref}}$ is the voltage across R_{ref}. Some considerations have to be made on both the choice of the current source and R_{ref}.

- **Current source (IDAC)**: the more current is sent through the resistors, the more

of the ADC range can be used, which leads to higher resolution. Nevertheless, the higher the current through a resistor, the more power it dissipates, which can lead to self-heating and subsequent measurement errors. A trade-off between these two factors has to be made. One way to reduce the possibility of self-heating is to constantly turn off the current generator when not measuring and turning it back on when needed, an operation that can be done quickly in PSoC devices.

- **Reference resistor**: the first thing to consider is to choose a resistor that does not overload the IDAC. In fact, the PSoC IDAC has a compliance voltage of $V_{DDA} - 1V$, which sets an upper limit on the voltage it can take at its output. This means that the series of R_{ref}, R and every other external resistance (e.g. wires, internal routings) cannot exceed

$$R_{MAX} = \frac{V_{compliance}}{I_{IDAC}} \tag{3.18}$$

  Another thing that is important to consider is the choice of a reference resistor similar to the resistance R being sensed. In fact, if the reference resistor and sensor are in the same part of the ADC transfer function, non-linearities in the ADC are canceled out.

As for the offset and gain errors, they are easily eliminated by applying equation 3.17, with the employment of a small trick: by setting the IDAC current to 0 mA, and measuring the voltages V^1_{off} and V^2_{off} across R and R_{ref} respectively, it is possible to quantify the overall offset given by ADC and signal chain; then, these values are simply subtracted from each voltage. The equation 3.17 becomes:

$$R = \frac{KK^{'}(V_R - V^1_{off})}{KK'(V_{R_{ref}} - V^2_{off})} \cdot R_{ref} \tag{3.19}$$

Where K and $K^{'}$ are the gain errors of the ADC and the IDAC respectively, and they reflect as multiplicative factors in the voltage expressions. Then

$$V_R = (I_{IDAC} + I_{off})R + ADC_{off} \tag{3.20}$$

$$V^1_{off} = (I_{off})R + ADC_{off} \tag{3.21}$$

$$V_{R_{ref}} = (I_{IDAC} + I_{off})R_{ref} + ADC_{off} \tag{3.22}$$

$$V^2_{off} = (I_{off})R_{ref} + ADC_{off} \tag{3.23}$$

The gain errors cancel out in the ratio, and the subtraction of the offset voltages nullifies the effects of both ADC voltage offset and IDAC current offset. Moreover, by repetitively tracking V_R, $V_{R_{ref}}$, V^1_{off}, and V^2_{off} and updating equation 3.19 at every measurement, any error associated to drifts is also removed.
Now the percentage error depends, in first approximation, on the tolerance of the reference resistor R_{ref} only.

The actual implementation of the reference resistor method in the context of this project introduces a slight variation, visible in Figure 3.15: the reference resistor for the sensor is substituted by a 10 $k\Omega$ potentiometer. This setup ensures flexibility on the choice of the proper reference, very important since in the optimal scenario it has to match the sensor resistance value, which is unknown at the beginning. Of course, to properly set the value of the potentiometer the user must be able to visualize it, and it has to be computed since it is not known in advance and can vary over time, just as for the sensor. Hence, a second reference resistor method has been implemented, with a 5 $k\Omega$ as reference resistance, being

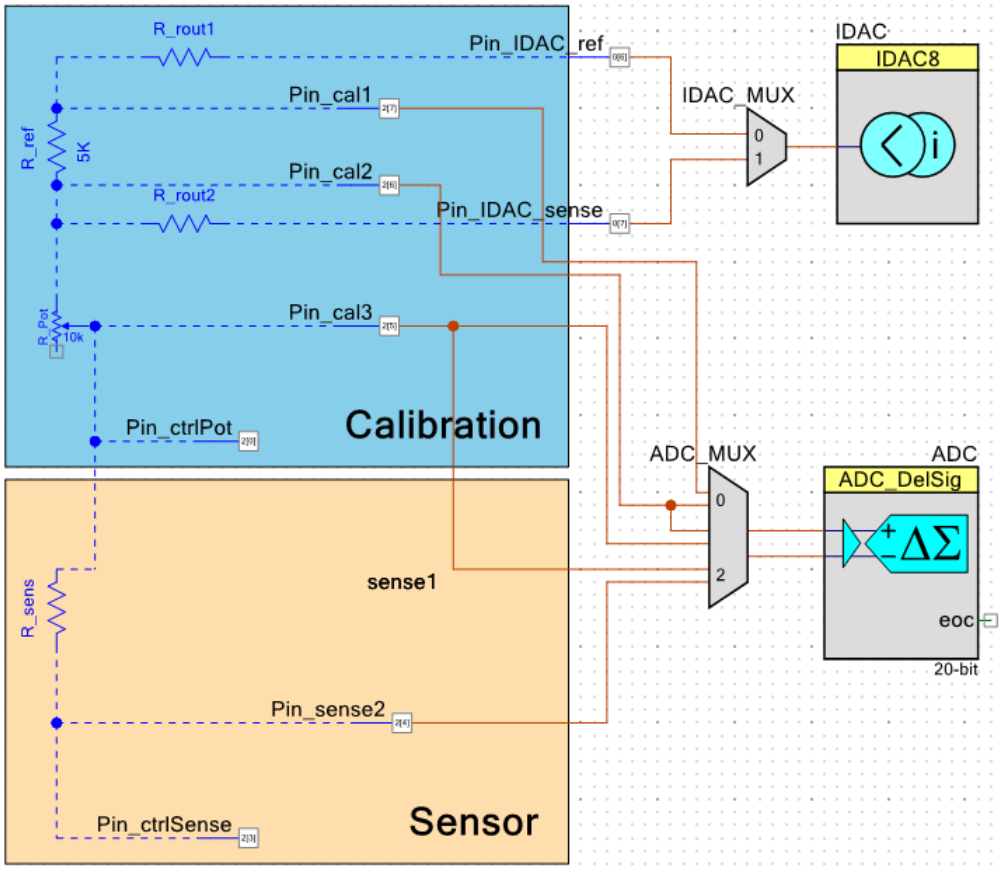

Figure 3.15: *Version of the reference resistor method implemented in this work. A potentiometer R_pot has been introduced as reference resistor to be able to tune it accordingly. Note that the GND pin of the potentiometer has been left floating, to avoid the creation of an undesired parallel path that would have complicated the computations. Wire resistances have been omitted (given they can be neglected) to keep the schematic clearer.*

in the middle of the potentiometer range. When not measuring the offsets, the value of the IDAC output current has been set to 100 μA. The current is then split thanks to an analog multiplexer into two alternative pathways: the reference pathway which consists in the series of the 5 $k\Omega$ reference resistance and the potentiometer, and the sensing pathway, which consists in the series of the potentiometer and the sensor. To make sure the current follows the desired path, the configuration of the circuit has to change dynamically. For this purpose, the two GPIO pins 'Pin_ctrlPot' and 'Pin_ctrlSense' drive modes can be reconfigured whenever needed as displayed in Table 3.3.
Lastly, a consideration on the range of resistance value that can be measured. As already said, the tension at the IDAC cannot exceed the compliance voltage $V_{DDA} - 1\ V = 4\ V$. From equation 3.18, being $I_{IDAC} = 100\ \mu A$, we get $R_{MAX} = 40\ k\Omega$. This is the maximum accepted value for the equivalent resistance of the path. Under the hypothesis of minimum value for the potentiometer (1 Ω, hence negligible), considering a PSoC internal routing resistance R_rout2 of 600 Ω [84] and negligible wire resistances, the maximum value of R that can be sensed is approximately 40 $k\Omega - 600\ \Omega = 39.4\ k\Omega$. Of course, in this way the reference resistor will be enormously far from the sensor resistance, hence the measurement will not be very accurate. The value of the IDAC current can be brought down to a minimum of 0.125 μA, but the smaller the current the less accurate are the measurements, and 100 μA was empirically found as a good trade-off.

Table 3.3: *'Pin_ctrlPot' and 'Pin_ctrlSense' GPIO pins drive mode configuration for the reference pathway and the sensing pathway.*

	Reference	**Sensing**
Pin_ctrlPot	Strong drive	High impedance analog
Pin_ctrlSense	High impedance analog	Strong drive

Firmware workflow

The part of code dedicated to the resistance readout is straightforward, and can be summarized as follows:

- If the user requests a calibration procedure to focus on setting the desired potentiometer value, the GPIO pins are configured according to the 'Reference' column of Table 3.3, channel 0 of the IDAC_MUX is selected and, for each resistor (i.e. R_ref and R_pot), the offset first and the actual voltages then are acquired; finally, the actual value of the potentiometer is computed according to equation 3.19. This whole process is repeated until the user is satisfied with the result.

- If the user instead starts a measurement procedure, every 500 ms (hence, at 2 Hz) the device will initially perform a single calibration step to acquire the actual value of the reference potentiometer (because it might not be known, or it may have changed even slightly with respect to what had been previously set by the user). The configuration of the GPIO pins is then changed to match the one reported in the 'Sensing' column of Table 3.3, channel 1 of the IDAC_MUX is selected and, for each resistor (i.e. R_pot and R_sens), the offset first and the actual voltages then are acquired; finally, the actual value of the sensor's resistance is computed according to equation 3.19. The voltages acquisitions and the resistance computation are repeated four times and the mean value is taken as the final result for R_sens. This whole process is repeated until the user stops the measurement procedure.

The firmware is fully available at: `https://github.com/AndreaRescalli/Tesi_Rescalli/tree/main/Thesis/RC-Meter.cydsn` and every step is commented to facilitate its comprehension.

3.3 Graphical user interface

3.3.1 Communication

The device is able to communicate data to and receive data from the GUI through a UART module, set to a baud rate of 9600 *bits per second*. Each single UART transaction consists in the transmission of 8 data bits and a final stop bit.
The current version of the GUI does not allow the user to change the settings of the FDC1004Q or other parameters such as the sample rate of the resistance readout. This is surely an important aspect that will be part of a future revision. Hence, the settings of the device and the FDC1004Q are defined in the firmware code, but they are communicated to the GUI environment upon connection because they are needed for some processing operations such as data visualization.
Any data that is transmitted or received is just a binary sequence. To be able to process these sequences, there's the need to discriminate between the different types of information

Table 3.4: *Headers and tails hexadecimal values, divided by class of information. The number inside the brackets after the class is the total number of bytes sent together, which is given by the sum of header, data and tail bytes.*

Class	Header	Tail	Brief description
Settings (5)	0x00	0x0F	FDC1004Q, PSoC capacitance and resistance readout data transmission frequencies.
Potentiometer calibration (8)	0x01	0x1F	Potentiometer data to be displayed during calibration phase; 4 bytes for integer part and 2 for decimal part.
FDC1004Q readout (8)	0x0A	0xFF	FDC1004Q measurement data; 4 bytes for integer part and 2 for decimal part.
PSoC capacitance readout (8)	0x0B	0xFF	PSoC capacitive measurement data; 4 bytes for integer part and 2 for decimal part.
PSoC resistance readout (14)	0x0C	0xFF	PSoC resistive measurement data; 4 bytes for integer part and 2 for decimal part for both sensor and potentiometer.

that are passed back and forth between the two entities. For this purpose, a system of unique header and tail bytes have been implemented and added to the information being transmitted, so that it is possible to recognize and verify the integrity of each piece of information exchanged: for instance, if the GUI is prepared to receive a particular header byte followed a certain amount of data bytes and a specific tail byte, but it receives a different number of bytes or the tail does not match the expected one, the information can be considered as corrupted, hence discarded. Table 3.4 summarizes the header and tail bytes used, divided by class of information, alongside the number of bytes involved in each exchange.

3.3.2 Application

This interface has been developed using PyQt5, a Python library that is based upon the C++ Qt free and open-source widget toolkit. Other Python libraries that are required for this application to work properly are:

- PyQtGraph, used for data visualization. Compared to other libraries such as matplotlib offers big advantages in terms of live interaction and fast update of plots; moreover, it is based on PyQt;
- pySerial, used to handle the communication between the GUI and the PSoC;
- pandas, used to manage the data export into a .csv file thanks to its capabilities in managing dictionaries and dataframes;
- Loguru, used to create a simple and efficient logging system to document the operations executed while the application is running.

The code is fully available at the following link: `https://github.com/AndreaRescalli/Tesi_Rescalli/tree/main/GUI`.

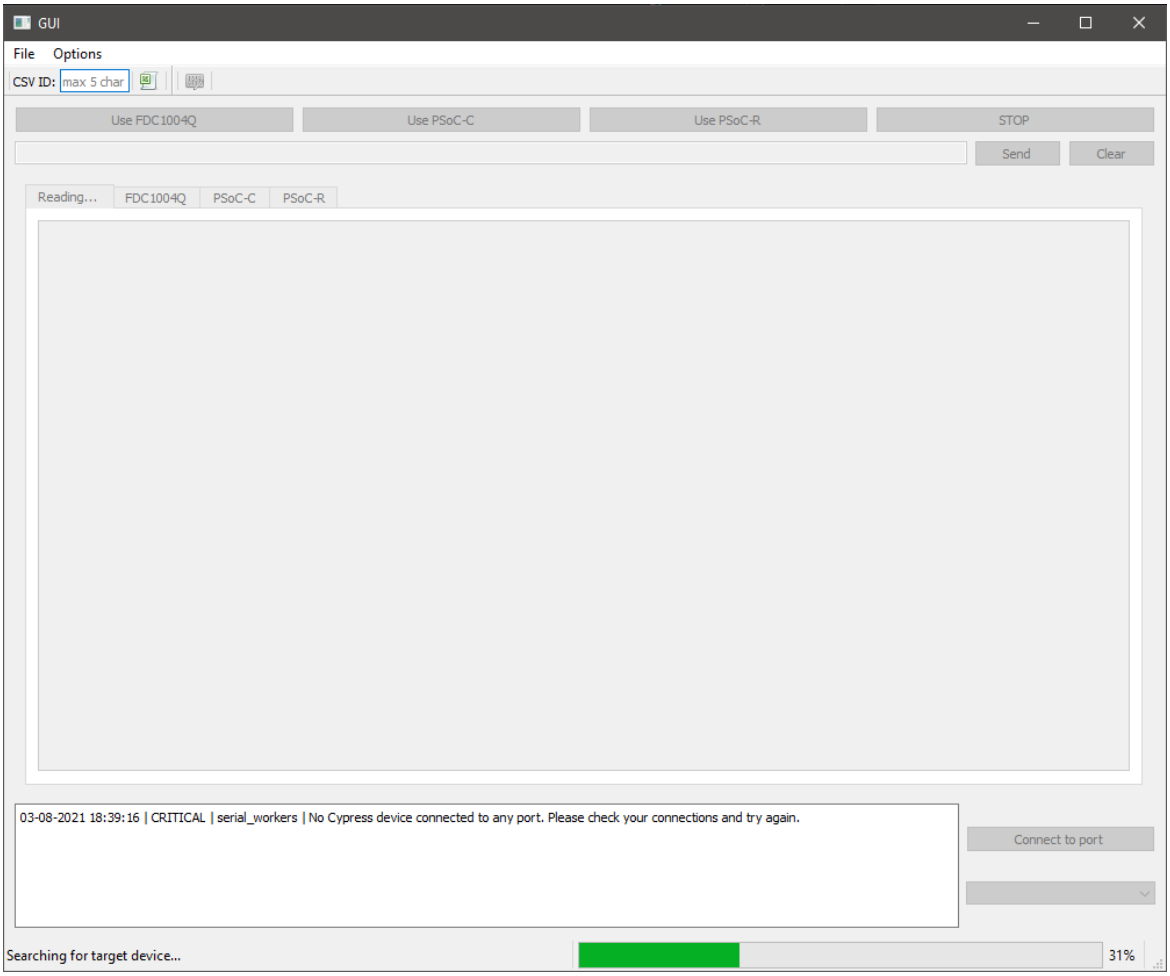

Figure 3.16: *The GUI is disabled: the progress bar on the bottom right indicates that the scan is running, while the debug terminal on the bottom left displays the error related to the situation of target device not found.*

As soon as the application is run, it starts to scan the list of serial ports to identify the one to which the target device is connected. The recognition event is based upon a question-answer mechanism: the GUI sends a predetermined character (i.e. *v*) on each active serial port, and waits for any incoming data; if this character is received by the PSoC, a predetermined string (i.e. *Thesis $$$*) is sent as an answer. When the GUI recognizes the string, it establishes the connection with the target device on the serial port in question, and any interaction with the application is enabled. If no answer, or a different one, is received, the user is notified with an error printed on the small debug terminal in the bottom left of the screen and the GUI remains unresponsive, as shown in Figure 3.16. The scan is repeated until a connection is established or the user closes the application. Once the GUI successfully connects with the target device, the interface is enabled and the user can choose whether to start a calibration of the potentiometer, a capacitive measurement with the FDC1004Q, a capacitive measurement with the PSoC relaxation oscillator circuit, or a resistive measurement. There's also a button to stop any running measurement.
The user can visualize data in two different ways: each readout procedure has its own dedicated graph tab that allows the visualization of the respective acquired data over time; alternatively, there is a tab (i.e. *Reading...*) that prints directly the numerical values.

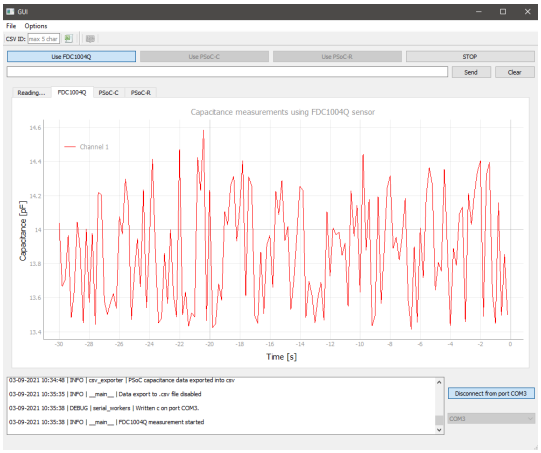

(a) *FDC1004Q capacitive measurements dedicated plot.*

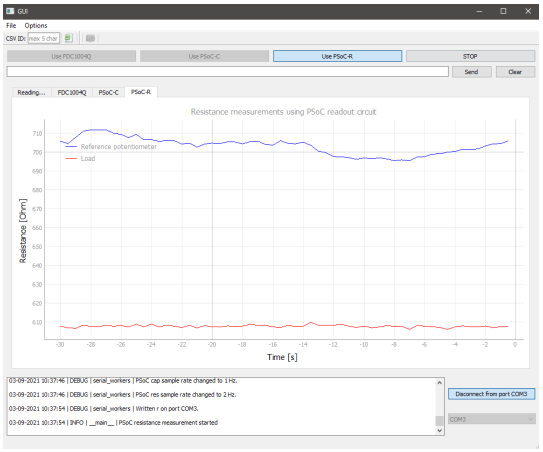

(b) *PSoC resistive measurements dedicated plot. Two lines can be seen: the blue one is the value of the reference potentiometer; the red one is the sensor's resistance.*

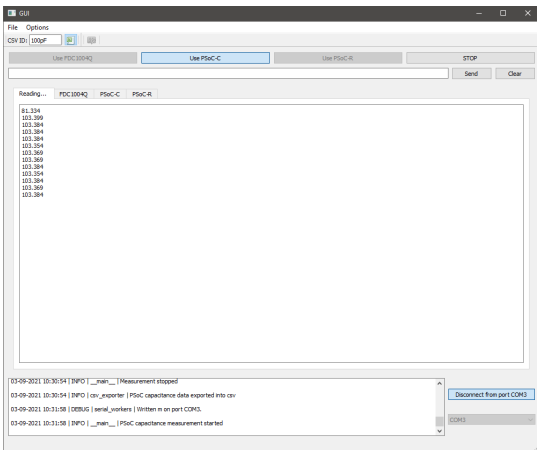

(c) *Reading... tab.*

Figure 3.17: *Examples of GUI's features. Figure (a) and (b) shows the dedicated tabs for the plot of the FDC1004Q and PSoC resistance measurements, respectively. Figure (c) displays the general purpose Reading... tab, where any incoming data is printed.*

The data collected during each acquisition are lost once a new one is run, unless the user decides to export them in a .csv file. It is also possible to assign an ID (of maximum 5 characters) to each .csv file to distinguish a measurement from another one.
Each operation performed during a single session (i.e. from the launch of the application to its closure) is tracked through a logging system and automatically saved in a .log file in case any investigation is needed. The most relevant information is also made available to the user in real time on the debug terminal. Figure 3.17 shows some of these features.

Chapter 4

Validation Tests and Experimental Results

This chapter presents the tests performed to validate the device alongside the results of the experiments run in laboratory.

4.1 Validation tests

A fundamental phase that precedes the employment of a device in any real-world application (such as a laboratory environment) is the establishment of its reliability as an instrument. Hence, the developed system has been tested on well-known capacitors and resistors to verify its accuracy. Results were compared to both nominal values and values measured with what has been considered a gold standard reference instrument, i.e. the FDC1004Q for capacitive measurements and a Wavetek Meterman 16XL digital multimeter [85] for resistive measurements.

4.1.1 Capacitance readout

The PSoC-based capacitance readout system has been tested on well-known capacitors ranging from 10 pF to 100 pF. In fact, values to be measured are expected to fall within the the pF range or even lower, being the concentration of toluene, butanone and hexanal in human exhaled breath really low, and being the polymeric film aimed at molecular recognition extremely thin (in the order of nanometers).
The results of these tests have been reported in Table 4.1. Each capacitor has been measured at first with the FDC1004Q to get a reference value; this value can be found in the second column of Table 4.1. Then, with the PSoC circuit, a 30-seconds acquisition has been performed, and the mean value alongside the percentage standard deviation have been reported in the third column of Table 4.1. The fourth column contains the accuracy error, which represents the deviation between the measurement of the reference instrument and the instrument to be tested, expressed as a percentage of the reference measurement. The formula is:

$$\epsilon = \frac{|y_x - y|}{y} \cdot 100 \tag{4.1}$$

Table 4.1: *Results of the capacitance readout validation tests. The measured values of the capacitors are reported as the mean value on 30-seconds measurements alongside the percentage standard deviation. The error ϵ is expressed as a percentage of the reference value.*

Nominal value	**Reference value**	**Measured value**		
$[pF]$	$[pF]$	Capacitor $[pF]$	ϵ	ΔC $[pF]$
10	13.7	$9.859 \pm 0.17\%$	28.0%	-3.841
20	21.9	$13.646 \pm 2.18\%$	37.7%	-8.254
30	33.8	$40.249 \pm 3.11\%$	19.1%	6.449
47	46.9	$56.737 \pm 1.80\%$	21.0%	9.837
56	55.4	$64.989 \pm 1.86\%$	17.3%	9.589
68	69.1	$75.804 \pm 2.02\%$	9.7%	6.704
100	101.8	$102.851 \pm 3.31\%$	1.0%	1.051

where y_x is the output of the PSoC circuit and y is the output of the FDC1004Q. The last column simply highlights the difference with respect to the reference value.

$$\Delta C = y_x - y \tag{4.2}$$

4.1.2 Resistance readout

The PSoC-based resistance readout system has been tested on well-known resistors ranging from 2.7 Ω to 10 $k\Omega$, below the maximum allowed value of resistance that can be measured (R_{sens} = 39.4 $k\Omega$, see 3.2.3). This is not a limitation, because prior to the employment of the PSoC device, the target sensor's resistance has been measured with the Wavetek Meterman 16XL digital multimeter to be sure its values were within the allowed range: maximum sensed resistances were in the order of 10^2 Ω, hence fully acceptable and within the tested range of values.
The results of these tests have been reported in Table 4.2. Each resistor has been measured at first with the Wavetek Meterman 16XL digital multimeter to get a reference value; this value can be found in the second column of Table 4.2 and is the one the instrument has stabilized to. Then, with the PSoC device, a set of 10 consecutive measurements has been performed for six different values (that can be found in the third column of Table 4.2) of the reference potentiometer, and the mean value alongside the percentage standard deviation have been reported in the fourth column of Table 4.2. The last column contains once again the accuracy error, computed with equation 4.1, where y_x is the output of the PSoC device and y the output of the reference instrument.

4.2 Experimental results

Despite the overall acceptable design of the developed capacitance readout circuit, capacitive measurements have not been performed. In fact, while this project was in its early stages, preliminary measurements were performed exploiting a device designed and realized by Davide Marzorati; this device is fully portable thanks to its Bluetooth communication capabilities

Table 4.2: *Results of the resistance readout validation tests. The nominal value has been reported alongside its percentage tolerance. The measured values of the resistors are reported as the mean value on 10 consecutive measurements alongside the percentage standard deviation. The error ϵ is expressed as a percentage of the reference value.*

Nominal value	**Reference value**	**Measured value**		
[Ω]	[Ω]	Potentiometer [Ω]	Resistor [Ω]	ϵ
$2.7 \pm 5\%$	3.4	10	$2.920 \pm 1.03\%$	14.1%
		100	$2.897 \pm 0.95\%$	14.8%
		1000	$2.906 \pm 0.88\%$	14.5%
		2500	$2.911 \pm 0.62\%$	14.4%
		5000	$2.919 \pm 0.97\%$	14.2%
		10000	$2.911 \pm 0.96\%$	14.4%
$8.2 \pm 5\%$	8.9	10	$8.759 \pm 8.71\%$	1.6%
		100	$8.561 \pm 0.40\%$	3.8%
		1000	$8.556 \pm 0.21\%$	3.9%
		2500	$8.542 \pm 0.15\%$	4.0%
		5000	$8.543 \pm 0.22\%$	4.0%
		10000	$8.546 \pm 0.31\%$	4.0%
$220 \pm 5\%$	218	10	$224.747 \pm 6.94\%$	3.1%
		100	$220.980 \pm 0.16\%$	1.4%
		1000	$220.744 \pm 0.07\%$	1.3%
		2500	$220.660 \pm 0.02\%$	1.2%
		5000	$220.640 \pm 0.01\%$	1.2%
		10000	$220.636 \pm 0.01\%$	1.2%
$600 \pm 5\%$	598	10	$606.045 \pm 0.25\%$	1.3%
		100	$607.006 \pm 0.06\%$	1.5%
		1000	$607.073 \pm 0.02\%$	1.5%
		2500	$606.985 \pm 0.02\%$	1.5%
		5000	$606.980 \pm 0.02\%$	1.5%
		10000	$606.944 \pm 0.01\%$	1.5%
$2000 \pm 5\%$	1981	10	$2022.335 \pm 0.46\%$	2.1%
		100	$2019.167 \pm 0.04\%$	1.9%
		1000	$2019.023 \pm 0.02\%$	1.9%
		2500	$2018.831 \pm 0.02\%$	1.9%
		5000	$2019.045 \pm 0.02\%$	1.9%
		10000	$2018.992 \pm 0.02\%$	1.9%
$10000 \pm 5\%$	9820	10	$9738.130 \pm 7.38\%$	0.8%
		100	$10005.709 \pm 0.24\%$	1.9%
		1000	$9986.350 \pm 0.03\%$	1.7%
		2500	$9984.020 \pm 0.03\%$	1.7%
		5000	$9983.781 \pm 0.01\%$	1.7%
		10000	$9984.747 \pm 0.02\%$	1.7%

and battery power supply, and uses the FDC1004Q as a reliable and accurate instrument to perform capacitive measurements. By monitoring the capacitance of the biosensors exposed

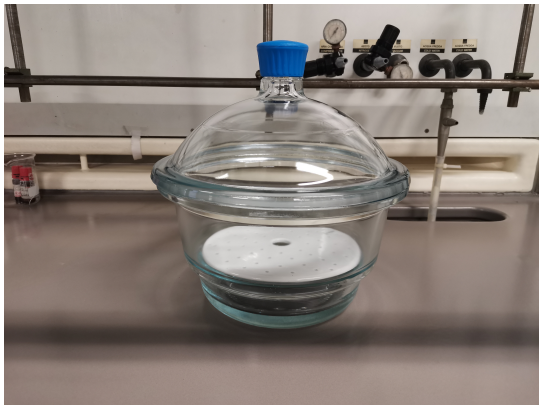

(a) *Glass chamber in which the experiments take place. The liquid is poured on the bottom of the chamber, below the white porous ceramic plate.*

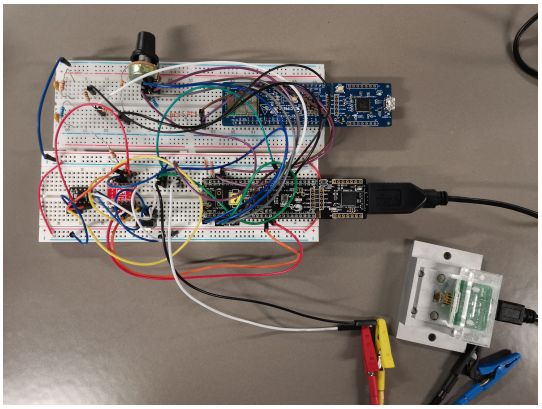

(b) *The all-in-one platform is attached to the device via a miniUSB-crocodile clips cable for baseline or post-exposure measurements.*

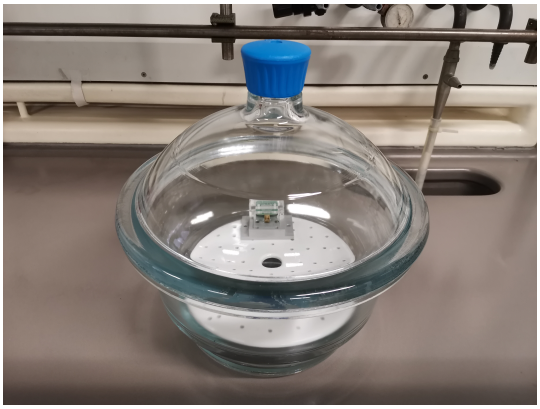

(c) *The all-in-one platform holding the sensor is put inside the chamber to be exposed to the analyte.*

Figure 4.1: *Different steps of the acquisition procedure.*

to the target analyte, a change in its value over time was expected; nevertheless, none of these preliminary experiments showed any variation during and/or after the exposure. Hence, to save time and resources the experiments carried out during this work focused only on resistive measurements.

4.2.1 Setup and acquisition protocol

The experiments have been carried out following a standard procedure:

1. First, a closed environment and static conditions have to be reproduced. To do so, a certain quantity of the target solvent (i.e. toluene, butanone or hexanal) is poured on the bottom of a glass chamber, where it is left evaporating until a saturated atmosphere is obtained (Figure 4.1a).

2. While waiting for the chamber to be filled with the target gas, the device is used to acquire the value of the resistance of the sensor prior to exposure. To do so, the MicruX all-in-one platform is connected to the developed device through a cable that has a miniUSB end to interface with the platform and four crocodile clips on the other end to interface with the readout circuitry, as visible in Figure 4.1b. These data provide

the so called *baseline* value of the sensor, $R0$. The acquisition is carried out for about a minute and the mean value is taken as $R0$.

3. After a sufficient amount of time, the all-in-one platform holding the electrode is put inside the saturated chamber (Figure 4.1c). Of course during this procedure the inside of the container is exposed for a moment to the outside air, but since the main point of the experiment isn't to measure a specific concentration of the target analyte this does not represent a big problem. For safety reasons, the experiments must be run under a laboratory hood to prevent any gas leakage. The sensor is kept exposed to the target analyte for 30 minutes, after which it is extracted from the chamber. In a particular experiment with the butanone-imprinted sensors, exposure for 6 and 16 hours have been investigated too.

4. As soon as the platform is extracted from the container, it is connected once again to the readout circuit and the resistance value of the sensor is measured. The main purpose is to identify a variation with respect to the baseline value, but the acquisition is carried on for a couple of minutes to get an idea of the desorption mechanism that the sensor undergo when exposed to air.

For each type of sensor, i.e. toluene-imprinted, butanone-imprinted and hexanal-imprinted, two versions have been prepared: one using an ED-IDE1-Au electrode and one using an ED-IDE3-Au electrode. Then, each sensor has undergone a specific set of experiments: it has been exposed three different times to the target analyte (in the results plots these trials are called A, B and C), then one time to the other analytes (e.g. the toluene-imprinted sensors have been exposed three times to toluene, one time to butanone and one time to hexanal).
Each set of experiments has been run with the same sensor to investigate its reuse capabilities. In order to do so, after each single experiment, the sensor must return to its initial state before it is put in the chamber for another trial. Therefore, the quantity of analyte that it has absorbed must be released. Given that the desorption process can require long times, to speed it up the sensor has been exposed to a flow of gaseous nitrogen.

4.2.2 Results

The results of all these experiments will now be presented, grouped by type of sensor and each group being divided into ED-IDE1-Au and ED-IDE3-Au.
The quantity under analysis is the precentage variation, over time, of the resistance value of the sensor after exposure with respect to the baseline value, and is computed as:

$$y = \frac{R - R0}{R0} \cdot 100 \tag{4.3}$$

Where R is the resistance value measured over time after exposure and $R0$ is the baseline, computed as described previously.

Toluene-imprinted sensors

According to the analysis presented in Subsection 3.1.3, these sensors are based on a MAA toluene-imprinted polymer matrix.
Figure 4.2a displays the results obtained with an ED-IDE1-Au electrode. The three curves TOL-A, TOL-B and TOL-C refers to the three toluene exposures and they show a similar, exponential-like response, with a mean peak variation with respect to $R0$ of $2.47\% \pm 0.77\%$; TOL-B shows a similar desorption behaviour to the other two in the initial moments while in

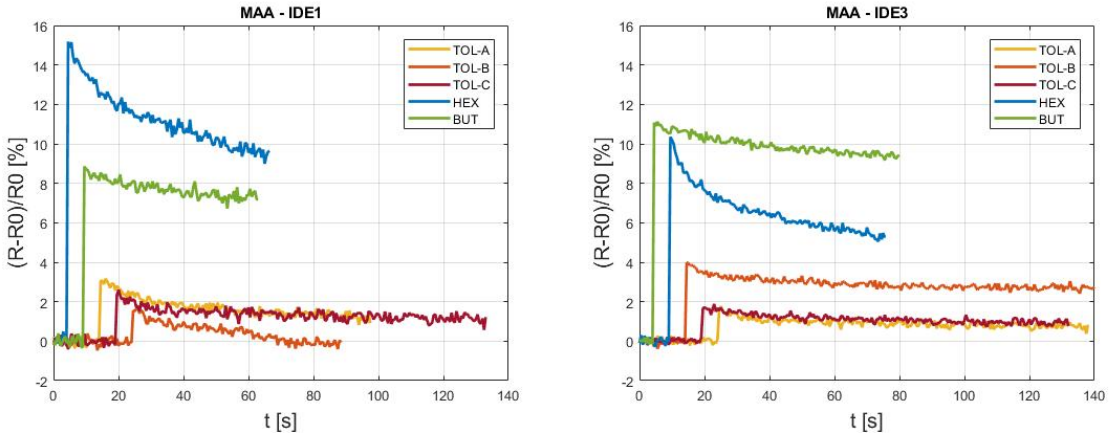

(a) *Toluene-imprinted ED-IDE1-Au sensor.* **(b)** *Toluene-imprinted ED-IDE3-Au sensor.*

Figure 4.2: *Toluene-imprinted sensors responses to 5 different experiments: each sensor has been exposed three times to toluene (TOL-A, TOL-B and TOL-C curves), one time to butanone (BUT) and one time to hexanal (HEX).*

the second part the curve steepens. Overall it can be said that the measurements are quite repeatable. The exposure to butanone and hexanal caused a much greater peak variation in the resistance value of the sensor, of 8.85% and 15.18% respectively. This is something counterintuitive, being the polymer designed to bind with toluene, but an explanation can be found in the behaviour of the MAA: despite being the functional monomer that maximizes the imprinting factor for toluene, from the graphs reported in Figure 3.4 it is evident how the toluene-imprinted polymer still absorbs more butanone than toluene itself (MAA-MIP for toluene can be considered MAA-NIP for butanone and hexanal). Nevertheless, this motivation still does not explain the behaviour of hexanal, which according to the same graphs is the least absorbed by a toluene-imprinted MAA polymer. Here, though, a clarification has to be done: the device measures the changes in resistance due to absorption, not the proper quantity of analyte absorbed. Hence, it is possible that despite being absorbed in lower quantities, the chemical composition of the hexanal induces bigger changes in the properties of the polymer, leading to higher variations of resistance. This hypothesis is supported also by the fact that the desorption process of hexanal is characterized by a very different time constant if compared to the other exponential curves. It has to be said that, with such a fast decay, the time needed to extract the platform from the chamber and connect it to the readout circuit is crucial: the hexanal response could have been even higher than the registered one. Figure 4.2b displays the results obtained with an ED-IDE3-Au electrode. Results similar to the ED-IDE1-Au sensor were found: the three toluene trials provided a mean peak variation of $2.54\% \pm 1.25\%$; this time the standard deviation is definitely more relevant due to TOL-B being a bit off with respect to the other two measurements. The peak response of the sensor to butanone is not very different from the previous case, 11.12%, while hexanal peak response is lower (10.35%), even if the shape of the curve still present a much faster decrease with respect to all the other curves.

One thing to be noted is the big step that occurs in each curve. Due to the nature of the communication between the device and the host machine (USB-based), the data can be acquired only before and after exposure: the absorption process cannot be monitored because the device must remain inside the insulated, closed chamber. Hence, there is a 30 minutes

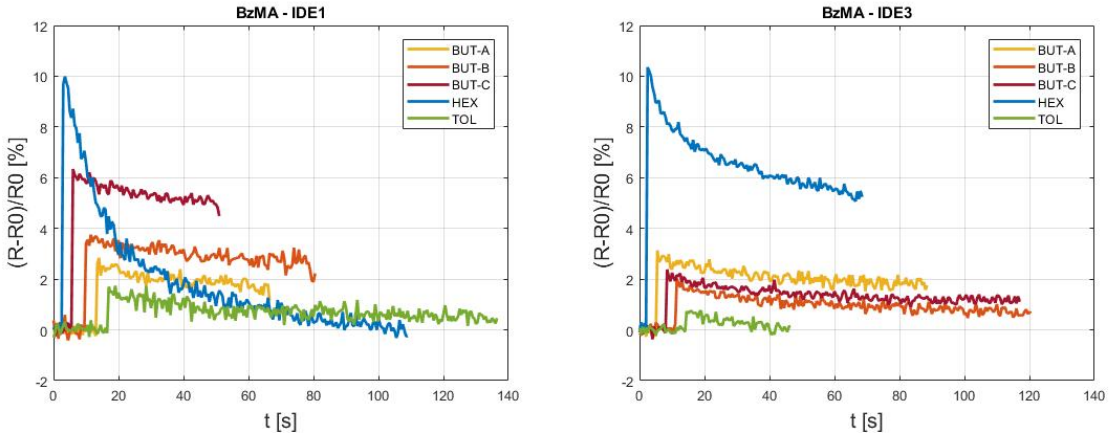

(a) *Butanone-imprinted ED-IDE1-Au sensor.* **(b)** *Butanone-imprinted ED-IDE3-Au sensor.*

Figure 4.3: *Butanone-imprinted sensors responses to 5 different experiments: each sensor has been exposed three times to butanone (BUT-A, BUT-B and BUT-C curves), one time to toluene (TOL) and one time to hexanal (HEX).*

gap between the first part of the curve and the second part, during which the sensor has changed its properties due to the contact with the analyte.

Butanone-imprinted sensors

According to the analysis presented in Subsection 3.1.3, these sensors are based on the BzMA butanone-imprinted polymer matrix.
Considering the graphs reported in Figure 3.4, BzMA-MIP for butanone shows the highest absorption properties if compared to BzMA-NIP for toluene and hexanal. It is then expected that these sensors would be able to easily discriminate the presence of butanone with respect to other gases.
Figure 4.3a displays the results obtained with an ED-IDE1-Au electrode. The three curves BUT-A, BUT-B and BUT-C refers to the three butanone exposures and they show a mean peak variation with respect to $R0$ of $4.31\% \pm 1.82\%$; despite showing a similar desorption behaviour, BUT-C is quite off with respect to the other two curves. Exposure to toluene provoked, as expected, the lowest peak variation (1.74%) amongst the three analyte, whereas hexanal is once again the compound that induced the highest variation, 9.99%. This was not expected based on the MIP-NIP absorption considerations, but can still find an explanation in the hypothesis made on the peculiar interactions between hexanal and the polymer: in fact, not only the response is higher but once again the desorption mechanism is the fastest of all, with a distinctive steep exponential curve.
Figure 4.3b displays the results obtained with an ED-IDE3-Au electrode. Results very similar to the ED-IDE1-Au sensor were found: the tree butanone trials provided a mean peak variation of $2.52\% \pm 0.56\%$; in this case the measurements shows a very repeatable behaviour, and the mean value is not offset by any trial. Toluene exposure generated a peak variation of 0.74% and hexanal induced a peak variation of 10.35%. Interestingly, despite being the hexanal peak variation almost the same between ED-IDE1-Au and ED-IDE3-Au, the desoprtion process is much faster in the first case.

For the butanone-imprinted sensors, also a different kind of experiment has been performed. Normally the sensor is kept in contact with the analyte for 30 minutes, but this time expo-

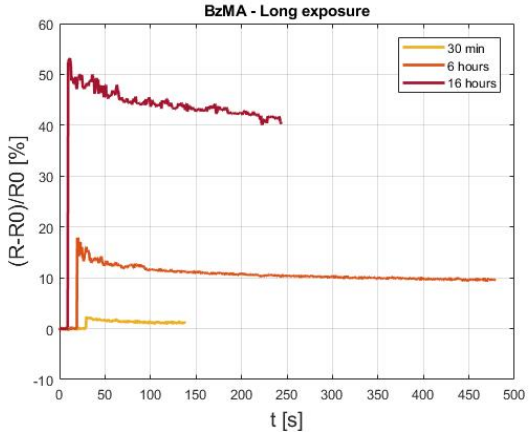

Figure 4.4: *Differences in the resistance variation of the butanone-imprinted ED-IDE3-Au sensor when exposed to butanone for 30 minutes, 6 hours and 16 hours.*

sures for 6 and 16 hours have been investigated too. Figure 4.4 displays the results obtained from these trials. 30 minutes peak variation (2.38%) is completely in line with the previous findings, highlighting the repeatability of the measurements; 6 hours exposure induced a variation of 17.90% and 16 hours exposure a variation of 53.22% with respect to the baseline value. These findings confirm that the absorption is a time-dependent process, and that the higher the exposure time, the higher the analyte absorbed and the subsequent resistance variation induced. On the other hand, longer desorption times are required for the sensor to return to it baseline condition, during which the sensor cannot be used, hence limiting its employment. These type of experiments couldn't be further investigated during this work because the prolonged exposure to such compound deteriorated the methacrylate component of the all-in-one platform, resulting in a permanent deformation of the instrument.

Hexanal-imprinted sensors

According to the analysis presented in Subsection 3.1.3, these sensors are based on the ChMA hexanal-imprinted polymer matrix.
Given that in the previous experiments hexanal was the compound inducing the highest peak resistance variation, even if the sensors were designed for other compounds, expectations are that for a hexanal-imprinted sensor the trend is going to be confirmed if not even accentuated. Figure 4.5a displays the results obtained with an ED-IDE1-Au electrode. The three curves HEX-A, HEX-B and HEX-C refers to the three hexanal exposures and they show a mean peak variation with respect to $R0$ of $24.48\% \pm 7.15\%$; the resistance variation is very high, as expected, but the standard deviation is not negligible and the behaviour of the exponential curves, despite being characterized by the fast decay already observed previously, is very different between the three trials. As a result, there is confidence to say that these three measurements are not as repeatable as they were for the toluene and butanone-imprinted sensors. Exposure to toluene and butanone provoked, as expected, much lower variations: 4.56% and 3.58% respectively.
Figure 4.5b displays the results obtained with an ED-IDE3-Au electrode. Responses to toluene (1.8%) and butanone (0.99%) are very low, in line with the results obtained with the ED-IDE1-Au. Nevertheless, this time the three hexanal trials showed a much lower mean peak variation, of $4.75\% \pm 2.12\%$, establishing for the first time a clear difference between ED-IDE1-Au and ED-IDE3-Au performances. This can be caused by two different (maybe even concurring) factors: the first one is that the polymer matrix is deposited onto the electrode

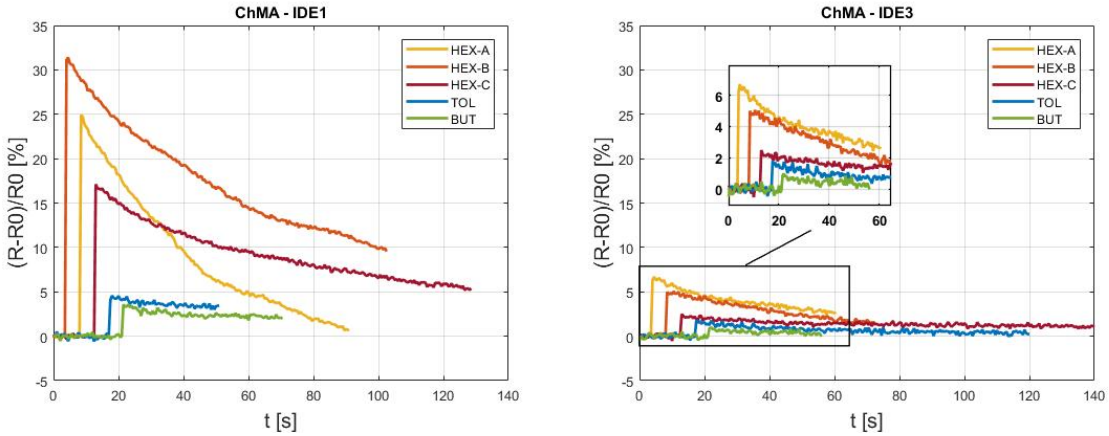

(a) *Hexanal-imprinted ED-IDE1-Au sensor.* **(b)** *Hexanal-imprinted ED-IDE3-Au sensor.*

Figure 4.5: *Hexanal-imprinted sensors responses to 5 different experiments: each sensor has been exposed three times to hexanal (HEX-A, HEX-B and HEX-C curves), one time to toluene (TOL) and one time to butanone (BUT).*

by drop coating, hence the nanotubes arrange themselves randomly on the active surface: sometimes they may aggregate, sometimes they may cover a greater portion of the active area of the electrodes, and this leads to different responses of the sensor. The second factor is related to the inconsistency of the hexanal responses observed throughout the experiments: in the toluene-imprinted sensors, between ED-IDE1-Au and ED-IDE3-Au there was a difference in the peak variation after the exposure; in the butanone-imprinted sensors instead, the peak value was the same but the shape of the exponential desorption process was visibly different; finally, in the hexanal-imprinted sensors, even the three trials performed on the same ED-IDE1-Au sensor were not consistent.

Chapter 5

Discussion and Future Developments

This project has been carried out with the aim of investigating new solutions that could be applied within the context of lung cancer screening. In particular, a system able to respond to toluene, butanone and hexanal gas mixtures, which have been identified as potential lung cancer biomarkers present in the exhaled breath of a subject, has been developed.
This system is based on chemosensors composed by a thin film molecularly imprinted polymer devoted to the recognition of the target analyte, deposited onto the active area of the transducer element, an interdigitated electrode produced by MicruX Technologies. Two different versions of these sensors have been realized by the team of Professor Francesco Cellesi and Francesco Bosatelli, and they are able to respond with a capacitance or a resistance variation when exposed to the target analyte.
The implemented electronic circuitry needed to interface with the sensors, to perform the measurements, to acquire the data and to transfer them to an external host machine, is based on the CY8CKIT-059 PSoC 5LP Prototyping Kit developed by Cypress Semiconductor Corporation. Three different readout solutions have been designed.
The first one includes a commercial sensor, the FDC1004Q capacitance-to-digital converter by Texas Instruments, to be used as a reference instrument to evaluate the performances of the PSoC-based capacitance readout circuit.
The second one exploits a relaxation oscillator circuit obtained with a comparator (internal to the PSoC), three external resistors and the capacitive biosensor. When the target analyte binds to the MIP layer, a change in the sensor's capacitance is induced and this reflects in a change of the oscillation frequency of the relaxation circuit. The output of the comparator feeds a series of PSoC's digital blocks devoted to the computation of the input signal's frequency, and from this information the unknown value of the sensor's capacitance can be retrieved and monitored during its variations over time. This solution has been validated on a set of commercial capacitors with known value, from 10 pF to 100 pF, covering the operational range of the reference instrument, i.e. the FDC1004Q capacitance-to-digital converter. The circuit seems to perform better in the higher portion of the range, especially around the 100 pF; for low values of capacitance, in fact, the percentage accuracy errors are quite high, with a peak error of 37.7% reached when measuring the 20 pF capacitor. Moreover, two distinct behaviours can be observed: up to 20 pF the designed circuit underestimates

the value of the capacitor, while from 30 pF there is an overestimation. Hence, despite showing stable measurement capabilities (the percentage standard deviations on 30-seconds acquisitions are low), and even if the acquired data are plausible and acceptable, these two factors highlight some limitations of the developed solution with respect to the commercial instrument; nevertheless, since capacitive measurements have been abandoned, all the efforts have been focused on improving the resistive side of this project.
The third solution is devoted to the resistance readout. The designed circuit is based on a four-wire configuration of the reference resistor method: a known current is injected, from the PSoC's IDAC component, through the series of an external reference resistor and the sensor; then, the voltages across the two resistances are measured by the PSoC's delta-sigma analog-to-digital converter and with a simple computation the value of the unknown sensor resistance can be derived. This solution has been validated on a set of commercial resistors with known value and tolerance, spanning from 2.7 Ω to 10 $k\Omega$. As a reference instrument, a Wavetek Meterman 16XL digital multimeter has been considered. The developed system showed excellent performances in the 10^2 to 10^4 Ω range, with a maximum percentage accuracy error of 3.1% found when the reference resistor (in this design, a potentiometer) was set very low (10 Ω) and distant from the value of the resistance to be measured (220 Ω in this particular measurement), hence in the worst conditions. The error with respect to the measurements obtained with the multimeter grows when the 10^1 Ω range is considered; nevertheless, there is confidence to say that here the developed system actually performs better than the reference instrument itself. As an example, for a nominal value of 2.7 $\Omega \pm 5\%$, the multimeter measures a resistance of 3.4 Ω, but this value is clearly off since it lies outside the tolerance range of the resistor itself. The implemented solution measures instead a resistance value of around 2.9 Ω, which is still slightly outside the 5% tolerance on the nominal value but considerably closer and more plausible.
A Python-based computer application has been realized for the user to interact with the system: there is the possibility to choose the type of measurement to be performed (and to stop any running acquisition), there are tabs dedicated to the real-time visualization of the data acquired by each individual readout solution, there is the possibility to run a calibration for the potentiometer to set the reference resistor at the most appropriate value and eventually the user can also enable the export of the data into a .csv file for further offline analysis.

Since the developed device has proven to be an accurate and reliable instrument especially for resistive measurements, it has been employed in a laboratory environment to investigate the behaviour of the resistive chemosensors exposed to toluene, butanone and hexanal. Capacitive measurements have been overlooked since preliminary results carried out with another device (developed by Davide Marzorati and based on the FDC1004Q as the measuring instrument) have shown poor if not null sensors responses.
The adopted protocol allowed to study the responses of each type of sensor (i.e. toluene-imprinted, butanone-imprinted and hexanal-imprinted), for each type of interdigitated electrode employed (i.e. ED-IDE1-Au and ED-IDE3-Au), to the target analyte it was designed for, and also their behaviour when exposed to the other two compounds, enriching the information about their selectivity.
The interaction of the target analyte with the recognition layer of the sensor induces a swelling process in the deposited polymer that increases the distance between the carbon nanotubes added to the matrix, disrupting the conducting pathways for the charge carriers. As a consequence, the conductivity of the material decreases and its resistance is expected to increase. In fact, all the experiments showed a positive variation of the resistance value of the sensor with respect to baseline. The adopted protocol also allowed to highlight an interesting

thing: each sensor reacted to any of the three compounds (hence, it could be inferred that the selectivity of the sensors is not very high), but with some peculiarities between them. Toluene-imprinted sensors showed a low response to toluene, a moderate variation when exposed to butanone and a high response followed by a fast decay when put in contact with hexanal. Butanone-imprinted sensors confirmed this trend, while for hexanal-imprinted sensors butanone was the compound that provoked the lowest variation out of the three analytes. These data shine a light on some underlying patterns that could be further investigated with new sets of experiments, maybe focused on acquiring data until the sensors resistance returns to the baseline value, to have information on the whole desorption process. Once a sufficient amount of observations are collected, a machine learning algorithm could be designed to see whether it is possible to recognize the compounds based on the response they induce in the sensors. Moreover, in this work the sensors were monitored one at a time, but for sure a combined analysis could only provide additional information to help the discrimination process. From the comparison of the results obtained with ED-IDE1-Au sensors and ED-IDE3-Au sensors, no big differences were found between the two categories, the only point of attention being the inconsistent behaviour of the hexanal response, especially in the hexanal-imprinted sensors. Nevertheless, this could be attributed to the randomness of the polymeric matrix distribution on the electrodes due to drop coating, which can cause different responses between a sensor and another one.
Finally, with another set of experiments run on the butanone-imprinted sensors, the correlation between the variation in resistance and the time of exposure was investigated. The sensor was put in contact with the target analyte for 30 minutes, 6 hours and 16 hours. A linear trend was observed, with the response intensity growing in function of the exposure time, but for sure more data need to be collected before jumping to any conclusion: a 3-observations batch is not sufficient. Unfortunately the all-in-one platform experienced permanent deformation after such a prolonged contact with the gaseous compound, compromising further investigations.

The biggest limitation of this work has been the impossibility to collect data during the absorption phase. This is a crucial piece of information needed to better characterize the responses of the sensors, but could not be acquired due to the nature of the communication protocol exploited by the device. In fact, the developed system is not self-powered, and the data acquired are transmitted in real-time via the PSoC's UART peripheral to the host machine, and not stored internally. For these reasons, the sensors can only be monitored before and after the exposure, when the PSoC is connected to (and powered by) the host machine via a USB cable: it is not physically possible to maintain a USB connection when the device is positioned inside a chamber that must remain closed to keep a saturated atmosphere inside. A possible solution will be to set up a battery-powered system endowed with either a Bluetooth communication protocol, to transmit data in real-time even during the absorption phase, or with an external memory to temporarily store the data and visualize them in a second moment, after the exposure.

The work carried out in this project represents only the first step towards the development of a lung cancer screening tool that could actually be applied in a clinical context; still, the results were promising. The next step in this direction would be to plan a set of experiments to measure known concentrations of the compounds: instead of putting the sensors in a saturated atmosphere, a hydraulic system of pumps and valves can be designed to create a controlled environment in which the sensors are in contact with a gas mixture of known composition. Only in this way it will be possible to find a relation between the sensors resistance

variations and the actual quantity of compound present in the air. This aspect is crucial to move towards a device able to quantify the presence of a certain substance in a gas sample of unknown composition.

Nevertheless, whether this type of analysis will ever crawl its way into clinical protocols is a big question mark. The literature is full of studies that for years have tried to find the best combination of VOCs to be used as lung cancer biomarkers alongside their respective concentrations, and new ones continue to be published. Still, a solution is far from being known, and each work claims its own findings. But as researchers, we should always seek for answers.

Bibliography

[1] Global Cancer Observatory: Cancer Today. International Agency for Research on Cancer. Data visualization tools for exploring the global cancer burden in 2020, 2020. (`https://gco.iarc.fr/today`, accessed March 2021).

[2] American Cancer Society. What is lung cancer?, 2019. (`https://www.cancer.org/cancer/lung-cancer/about/what-is.html`, accessed March 2021).

[3] Kentaro Inamura. Lung cancer: understanding its molecular pathology and the 2015 WHO classification. *Frontiers in Oncology*, 7:193, 2017.

[4] K. S. Park, M. C. Liang, D. M. Raiser, R. Zamponi, R. R. Roach, S. J. Curtis, Z. Walton, B. E. Schaffer, C. M. Roake, A. F. Zmoos, C. Kriegel, K. K. Wong, J. Sage, and C. F. Kim. Characterization of the cell of origin for small cell lung cancer. *Cell Cycle*, 10(16):2806–2815, 2011.

[5] Sean Blandin Knight, Phil A. Crosbie, Haval Balata, Jakub Chudziak, Tracy Hussell, and Caroline Dive. Progress and prospects of early detection in lung cancer. *Open Biology*, 7(9):170070, sep 2017.

[6] Neil Bannister and John Broggio. One-year net cancer survival for bladder, breast, colorectal, kidney, lung, melanoma, ovary, prostate and uterus, by stage at diagnosis, 2016. (`UK Office for National Statistics`, accessed March 2021).

[7] Chi-Fu Jeffrey Yang, Derek Y. Chan, Paul J. Speicher, Brian C. Gulack, Xiaofei Wang, Matthew G. Hartwig, Mark W. Onaitis, Betty C. Tong, Thomas A. D'Amico, Mark F. Berry, and David H. Harpole. Role of adjuvant therapy in a population-based cohort of patients with early-stage small-cell lung cancer. *Journal of Clinical Oncology*, 34(10):1057–1064, apr 2016.

[8] World Health Organization. *Guide to cancer early diagnosis*. WHO Document Production Services, 2017.

[9] National Comprehensive Cancer Network. NCCN guidelines for patients: Lung cancer screening, 2020. (`https://www.nccn.org/patients/guidelines/content/PDF/lung_screening-patient.pdf`, accessed April 2021).

[10] Sean Blandin Knight, Phil A Crosbie, Haval Balata, Jakub Chudziak, Tracy Hussell, and Caroline Dive. Progress and prospects of early detection in lung cancer. *Open Biology*, 7(9):170070, September 2017.

[11] S Sone, F Li, ZG Yang, T Honda, Y Maruyama, S Takashima, M Hasegawa, S Kawakami, K Kubo, M Haniuda, et al. Results of three-year mass screening programme for lung cancer using mobile low-dose spiral computed tomography scanner. *British Journal of Cancer*, 84(1):25–32, 2001.

[12] Robert S. Fontana, David R. Sanderson, Lewis B. Woolner, William F. Taylor, W. Eugene Miller, John R. Muhm, et al. Lung cancer screening: the Mayo program. *Journal of Occupational Medicine*, 28(8):746–750, August 1986.

[13] John K. Frost, Wilmot C. Ball Jr, Morton L. Levin, Melvyn S. Tockman, R. Robinson Baker, Darryl Carter, Joseph C. Eggleston, Yener S. Erozan, Prabodh K. Gupta, Nagi F. Khouri, et al. Early lung cancer detection: results of the initial (prevalence) radiologic and cytologic screening in the Johns Hopkins study. *American Review of Respiratory Disease*, 130(4):549–554, 1984.

[14] Philip C. Prorok, Gerald L. Andriole, Robert S. Bresalier, Saundra S. Buys, David Chia, E. David Crawford, Ronald Fogel, Edward P. Gelmann, Fred Gilbert, Marsha A Hasson, et al. Design of the prostate, lung, colorectal and ovarian (PLCO) cancer screening trial. *Controlled Clinical Trials*, 21(6):273S–309S, 2000.

[15] Frederick J. Larke, Randell L. Kruger, Christopher H. Cagnon, Michael J. Flynn, Michael M. McNitt-Gray, Xizeng Wu, Phillip F. Judy, and Dianna D. Cody. Estimated radiation dose associated with low-dose chest CT of average-size participants in the National Lung Screening Trial. *American Journal of Roentgenology*, 197(5):1165–1169, November 2011.

[16] Dag Wormanns, Karl Ludwig, Florian Beyer, Walter Heindel, and Stefan Diederich. Detection of pulmonary nodules at multirow-detector CT: effectiveness of double reading to improve sensitivity at standard-dose and low-dose chest CT. *European Radiology*, 15(1):14–22, November 2005.

[17] Maurizio Infante, Silvio Cavuto, Fabio Romano Lutman, Giorgio Brambilla, Giuseppe Chiesa, Giovanni Ceresoli, Eliseo Passera, Enzo Angeli, Maurizio Chiarenza, Giuseppe Aranzulla, Umberto Cariboni, Valentina Errico, Francesco Inzirillo, Edoardo Bottoni, Emanuele Voulaz, Marco Alloisio, Anna Destro, Massimo Roncalli, Armando Santoro, and Gianluigi Ravasi. A randomized study of lung cancer screening with spiral computed tomography. *American Journal of Respiratory and Critical Care Medicine*, 180(5):445–453, September 2009.

[18] Maurizio Infante, Silvio Cavuto, Fabio Romano Lutman, Eliseo Passera, Maurizio Chiarenza, Giuseppe Chiesa, Giorgio Brambilla, Enzo Angeli, Giuseppe Aranzulla, Arturo Chiti, Marta Scorsetti, Pierina Navarria, Raffaele Cavina, Michele Ciccarelli, Massimo Roncalli, Anna Destro, Edoardo Bottoni, Emanuele Voulaz, Valentina Errico, Giorgio Ferraroli, Giovanna Finocchiaro, Luca Toschi, Armando Santoro, and Marco Alloisio. Long-term follow-up results of the DANTE trial, a randomized study of lung cancer screening with spiral computed tomography. *American Journal of Respiratory and Critical Care Medicine*, 191(10):1166–1175, May 2015.

[19] Zaigham Saghir, Asger Dirksen, Haseem Ashraf, Karen Skjøldstrup Bach, John Brodersen, Paul Frost Clementsen, Martin Døssing, Hanne Hansen, Klaus Fuglsang Kofoed, Klaus Richter Larsen, Jann Mortensen, Jakob Fraes Rasmussen, Niels Seersholm, Birgit Guldhammer Skov, Hanne Thorsen, Philip Tønnesen, and Jesper Holst Pedersen. CT screening for lung cancer brings forward early disease. The randomised Danish Lung Cancer Screening Trial: status after five annual screening rounds with low-dose CT. *Thorax*, 67(4):296–301, 2012.

[20] National Lung Screening Trial Research Team. Reduced lung-cancer mortality with low-dose computed tomographic screening. *New England Journal of Medicine*, 365(5):395–409, August 2011.

[21] Douglas E. Wood, Ella A. Kazerooni, Scott L. Baum, George A. Eapen, David S. Ettinger, Lifang Hou, David M. Jackman, Donald Klippenstein, Rohit Kumar, Rudy P. Lackner, Lorriana E. Leard, Inga T. Lennes, Ann N.C. Leung, Samir S. Makani, Pierre P. Massion, Peter Mazzone, Robert E. Merritt, Bryan F. Meyers, David E. Midthun, Sudhakar Pipavath, Christie Pratt, Chakravarthy Reddy, Mary E. Reid, Arnold J. Rotter, Peter B. Sachs, Matthew B. Schabath, Mark L. Schiebler, Betty C. Tong, William D. Travis, Benjamin Wei, Stephen C. Yang, Kristina M. Gregory, and Miranda Hughes. Lung cancer screening, version 3.2018, NCCN clinical practice guidelines in oncology. *Journal of the National Comprehensive Cancer Network*, 16(4):412–441, April 2018.

[22] Samuel G. Armato, Rachael Y. Roberts, Masha Kocherginsky, Denise R. Aberle, Ella A. Kazerooni, Heber MacMahon, Edwin J.R. van Beek, David Yankelevitz, Geoffrey McLennan, Michael F. McNitt-Gray, Charles R. Meyer, Anthony P. Reeves, Philip Caligiuri, Leslie E. Quint, Baskaran Sundaram, Barbara Y. Croft, and Laurence P. Clarke. Assessment of radiologist performance in the detection of lung nodules: Dependence on the definition of "truth". *Academic Radiology*, 16(1):28–38, 2009.

[23] American College of Radiology. Lung CT screening Reporting And Data System (Lung-RADS). (`https://www.acr.org/Clinical-Resources/Reporting-and-Data-Systems/Lung-Rads`, accessed April 2021).

[24] Badera Al Mohammad, Patrick C. Brennan, and Claudia Mello-Thoms. A review of lung cancer screening and the role of computer-aided detection. *Clinical Radiology*, 72(6):433–442, 2017.

[25] Annette G. Dent, Tom G. Sutedja, and Paul V. Zimmerman. Exhaled breath analysis for lung cancer. *Journal of Thoracic Disease*, 5(5):S540–S550, October 2013.

[26] Peter J Mazzone. Analysis of volatile organic compounds in the exhaled breath for the diagnosis of lung cancer. *Journal of Thoracic Oncology*, 3(7):774–780, July 2008.

[27] Meggie Hakim, Yoav Y. Broza, Orna Barash, Nir Peled, Michael Phillips, Anton Amann, and Hossam Haick. Volatile organic compounds of lung cancer and possible biochemical pathways. *Chemical Reviews*, 112(11):5949–5966, 2012. PMID: 22991938.

[28] Orna Barash, Nir Peled, Ulrike Tisch, Paul A. Bunn, Fred R. Hirsch, and Hossam Haick. Classification of lung cancer histology by gold nanoparticle sensors. *Nanomedicine: Nanotechnology, Biology and Medicine*, 8(5):580–589, 2012.

[29] Min Wang, Jiajing Sheng, Qian Wu, Yingchang Zou, Yanjie Hu, Kejing Ying, Hao Wan, and Ping Wang. Confounding effect of benign pulmonary diseases in selecting volatile organic compounds as markers of lung cancer. *Journal of breath research*, 12:046013, September 2018.

[30] Davide Marzorati, Luca Mainardi, Giulia Sedda, Roberto Gasparri, Lorenzo Spaggiari, and Pietro Cerveri. A review of exhaled breath: a key role in lung cancer diagnosis. *Journal of Breath Research*, 13(3):034001, apr 2019.

[31] Harvey Pass Gerardo Velez. A review of exhaled volatile organic compounds as biomarkers for thoracic malignancies. *American Journal of Biomedical and Life Sciences*, 8(6):231–247, 2020.

[32] Diana Poli, Paolo Carbognani, Massimo Corradi, Matteo Goldoni, Olga Acampa, Bruno Balbi, Luca Bianchi, Michele Rusca, and Antonio Mutti. Exhaled volatile organic compounds in patients with non-small cell lung cancer: cross sectional and nested short-term follow-up study. *Respiratory Research*, 6(1):71, 2005.

[33] Michael Phillips, Nasser Altorki, John H. M. Austin, Robert B. Cameron, Renee N. Cataneo, Joel Greenberg, Robert Kloss, Roger A. Maxfield, Muhammad I. Munawar, Harvey I. Pass, Asif Rashid, William N. Rom, and Peter Schmitt. Prediction of lung cancer using volatile biomarkers in breath. *Cancer Biomarkers*, 3(2):95–109, 2007.

[34] Xue AU Li, Dan D. AU Huang, Rui AU Du, Zhi J. AU Zhang, Chak K. AU Chan, Zheng X. AU Huang, and Zhen AU Zhou. Real-time breath analysis by using secondary nanoelectrospray ionization coupled to high resolution mass spectrometry. *Journal of Visualized Experiments*, (133):e56465, 2018.

[35] Andreas Wehinger, Alex Schmid, Sergei Mechtcheriakov, Maximilian Ledochowski, Christoph Grabmer, Guenther A. Gastl, and Anton Amann. Lung cancer detection by proton transfer reaction mass-spectrometric analysis of human breath gas. *International Journal of Mass Spectrometry*, 265(1):49–59, 2007.

[36] Amel Bajtarevic, Clemens Ager, Martin Pienz, Martin Klieber, Konrad Schwarz, Magdalena Ligor, Tomasz Ligor, Wojciech Filipiak, Hubert Denz, Michael Fiegl, Wolfgang Hilbe, Wolfgang Weiss, Peter Lukas, Herbert Jamnig, Martin Hackl, Alfred Haidenberger, Boguslaw Buszewski, Wolfram Miekisch, Jochen Schubert, and Anton Amann. Noninvasive detection of lung cancer by analysis of exhaled breath. *BMC Cancer*, 9(1):348, 2009.

[37] P. Martìnez-Lozano and J. Fernàndez de la Mora. Electrospray ionization of volatiles in breath. *International Journal of Mass Spectrometry*, 265(1):68–72, 2007.

[38] Xue Li, Lei Huang, Hui Zhu, and Zhen Zhou. Direct human breath analysis by secondary nano-electrospray ionization ultrahigh-resolution mass spectrometry: Importance of high mass resolution and mass accuracy. *Rapid Communications in Mass Spectrometry*, 31(3):301–308, January 2017.

[39] M Westhoff, P Litterst, L Freitag, W Urfer, S Bader, and J-I Baumbach. Ion mobility spectrometry for the detection of volatile organic compounds in exhaled breath of patients with lung cancer: results of a pilot study. *Thorax*, 64(9):744–748, 2009.

[40] J. C. Reynolds, G. J. Blackburn, C. Guallar-Hoyas, V. H. Moll, V. Bocos-Bintintan, G. Kaur-Atwal, M. D. Howdle, E. L. Harry, L. J. Brown, C. S. Creaser, and C. L. P. Thomas. Detection of volatile organic compounds in breath using thermal desorption electrospray ionization-ion mobility-mass spectrometry. *Analytical Chemistry*, 82(5):2139–2144, March 2010.

[41] Wouter H. Geffen, Kevin Lamote, Adrien Costantini, Lizza Hendriks, Najib Rahman, Torsten Blum, and Jan Meerbeeck. The electronic nose: Emerging biomarkers in lung cancer diagnostics. *Breathe*, 15:e135–e141, December 2019.

[42] Peter J Mazzone, Xiao-Feng Wang, Yaomin Xu, Tarek Mekhail, Mary C Beukemann, Jie Na, Jonathan W Kemling, Kenneth S Suslick, and Madhu Sasidhar. Exhaled breath analysis with a colorimetric sensor array for the identification and characterization of lung cancer. *Journal of Thoracic Oncology*, 7(1):137–142, 2012.

[43] Xianhua Zhong, Dan Li, Wei Du, Mengqiu Yan, You Wang, Danqun Huo, and Changjun Hou. Rapid recognition of volatile organic compounds with colorimetric sensor arrays for lung cancer screening. *Analytical and Bioanalytical Chemistry*, 410(16):3671–3681, 2018.

[44] Liang Feng, Christopher J. Musto, Jonathan W. Kemling, Sung H. Lim, Wenxuan Zhong, and Kenneth S. Suslick. Colorimetric sensor array for determination and identification of toxic industrial chemicals. *Anal. Chem.*, 82(22):9433–9440, November 2010.

[45] Corrado Di Natale, Roberto Paolesse, and Arnaldo D'Amico. Metalloporphyrins based artificial olfactory receptors. *Sensors and Actuators B: Chemical*, 121(1):238–246, 2007. Special Issue: 25th Anniversary of Sensors and Actuators B: Chemical.

[46] Corrado Di Natale, Antonella Macagnano, Eugenio Martinelli, Roberto Paolesse, Giuseppe D'Arcangelo, Claudio Roscioni, Alessandro Finazzi-Agrò, and Arnaldo D'Amico. Lung cancer identification by the analysis of breath by means of an array of non-selective gas sensors. *Biosensors and Bioelectronics*, 18(10):1209–1218, 2003.

[47] Arnaldo D'Amico, Giorgio Pennazza, Marco Santonico, Eugenio Martinelli, Claudio Roscioni, Giovanni Galluccio, Roberto Paolesse, and Corrado Di Natale. An investigation on electronic nose diagnosis of lung cancer. *Lung Cancer*, 68(2):170–176, 2010.

[48] Madara Tirzite, Māris Bukovskis, Gunta Strazda, Normunds Jurka, and Immanuels Taivans. Detection of lung cancer with electronic nose and logistic regression analysis. *Journal of Breath Research*, 13(1):016006, nov 2018.

[49] Roberto F. Machado, Daniel Laskowski, Olivia Deffenderfer, Timothy Burch, Shuo Zheng, Peter J. Mazzone, Tarek Mekhail, Constance Jennings, James K. Stoller, Jacqueline Pyle, Jennifer Duncan, Raed A. Dweik, and Serpil C. Erzurum. Detection of lung cancer by sensor array analyses of exhaled breath. *American journal of respiratory and critical care medicine*, 171:1286–91, Jun 2005.

[50] Chengxiang Wang, Longwei Yin, Luyuan Zhang, Dong Xiang, and Rui Gao. Metal oxide gas sensors: Sensitivity and influencing factors. *Sensors*, 10(3):2088–2106, 2010.

[51] Rens Van de Goor, Michel van Hooren, Anne-Marie Dingemans, Bernd Kremer, and Kenneth Kross. Training and validating a portable electronic nose for lung cancer screening. *Journal of Thoracic Oncology*, 13(5):676–681, 2018.

[52] Gang Peng, Ulrike Tisch, Orna Adams, Meggie Hakim, Nisrean Shehada, Yoav Y. Broza, Salem Billan, Roxolyana Abdah-Bortnyak, Abraham Kuten, and Hossam Haick. Diagnosing lung cancer in exhaled breath using gold nanoparticles. *Nature Nanotechnology*, 4(10):669–673, 2009.

[53] Giuseppe Vasapollo, Roberta Del Sole, Lucia Mergola, Maria Rosaria Lazzoi, Anna Scardino, Sonia Scorrano, and Giuseppe Mele. Molecularly imprinted polymers: Present and future prospective. *International Journal of Molecular Sciences*, 12(9):5908–5945, 2011.

[54] Joseph J. BelBruno. Molecularly imprinted polymers. *Chemical Reviews*, 119(1):94–119, January 2019.

[55] Karsten Haupt and Klaus Mosbach. Molecularly imprinted polymers and their use in biomimetic sensors. *Chem. Rev.*, 100(7):2495–2504, July 2000.

[56] Karsten Haupt, Paulina X. Medina Rangel, and Bernadette Tse Sum Bui. Molecularly imprinted polymers: Antibody mimics for bioimaging and therapy. *Chemical Reviews*, 120(17):9554–9582, September 2020.

[57] Lars Andersson, Börje Sellergren, and Klaus Mosbach. Imprinting of amino acid derivatives in macroporous polymers. *Tetrahedron Letters*, 25(45):5211–5214, 1984.

[58] G Wulff, A Sarhan, and K Zabrocki. Enzyme-analogue built polymers and their use for the resolution of racemates. *Tetrahedron Letters*, 14(44):4329–4332, 1973.

[59] Ching-Chiang Hwang and Wen-Chien Lee. Chromatographic characteristics of cholesterol-imprinted polymers prepared by covalent and non-covalent imprinting methods. *Journal of Chromatography A*, 962(1):69–78, 2002.

[60] Mehmet Dinc, Cem Esen, and Boris Mizaikoff. Recent advances on core-shell magnetic molecularly imprinted polymers for biomacromolecules. *TrAC Trends in Analytical Chemistry*, 114:202–217, 2019.

[61] Sergey A. Piletsky, Håkan S. Andersson, and Ian A. Nicholls. Combined hydrophobic and electrostatic interaction-based recognition in molecularly imprinted polymers. *Macromolecules*, 32(3):633–636, February 1999.

[62] Elena Benito-Peña, Sofia Martins, Guillermo Orellana, and María Cruz Moreno-Bondi. Water-compatible molecularly imprinted polymer for the selective recognition of fluoroquinolone antibiotics in biological samples. *Analytical and Bioanalytical Chemistry*, 393(1):235–245, 2009.

[63] A. Hulanicki, S. Glab, and F. Ingman. Chemical sensors: definitions and classification. *Pure and Applied Chemistry*, 63(9):1247–1250, 1991.

[64] Nadja Leibl, Karsten Haupt, Carlo Gonzato, and Luminita Duma. Molecularly imprinted polymers for chemical sensing: A tutorial review. *Chemosensors*, 9(6), 2021.

[65] National Center for Biotechnology Information. PubChem compound summary for CID 1140, Toluene, 2021. (`https://pubchem.ncbi.nlm.nih.gov/compound/Toluene`, accessed July 2021).

[66] Joanna Rudnicka, Tomasz Kowalkowski, Tomasz Ligor, and Boguslaw Buszewski. Determination of volatile organic compounds as biomarkers of lung cancer by SPME-GC-TOF/MS and chemometrics. *Journal of Chromatography B*, 879(30):3360–3366, 2011.

[67] Boguslaw Buszewski, Tomasz Ligor, Tadeusz Jezierski, Anna Wenda-Piesik, Marta Walczak, and Joanna Rudnicka. Identification of volatile lung cancer markers by gas chromatography-mass spectrometry: comparison with discrimination by canines. *Analytical and Bioanalytical Chemistry*, 404(1):141–146, 2012.

[68] National Center for Biotechnology Information. PubChem compound summary for CID 6569, Methyl ethyl ketone, 2021. (`https://pubchem.ncbi.nlm.nih.gov/compound/Methyl-ethyl-ketone`, accessed July 2021).

[69] World Health Organization and International Programme on Chemical Safety. Methyl ethyl ketone / published under the joint sponsorship of the United Nations Environment Programme, the International Labour Organisation, and the World Health Organization, 1993.

[70] Xiao-An Fu, Mingxiao Li, Ralph J. Knipp, Michael H. Nantz, and Michael Bousamra. Noninvasive detection of lung cancer using exhaled breath. *Cancer Medicine*, 3(1):174–181, 2014.

[71] National Center for Biotechnology Information. PubChem compound summary for CID 6184, Hexanal, 2021. (`https://pubchem.ncbi.nlm.nih.gov/compound/Hexanal`, accessed July 2021).

[72] Sajjad Janfaza, Maryam Banan Nojavani, Maryam Nikkhah, Taher Alizadeh, Ali Esfandiar, and Mohammad Reza Ganjali. A selective chemiresistive sensor for the cancer-related volatile organic compound hexanal by using molecularly imprinted polymers and multiwalled carbon nanotubes. *Microchimica Acta*, 186(3):137, 2019.

[73] Patricia Fuchs, Christian Loeseken, Jochen K. Schubert, and Wolfram Miekisch. Breath gas aldehydes as biomarkers of lung cancer. *International Journal of Cancer*, 126(11):2663–2670, 2010.

[74] MicruX Technologies. Thin-film interdigitated electrodes. (`www.micruxfluidic.com`, accessed July 2021).

[75] MicruX Technologies. All-in-one platform. (`www.micruxfluidic.com`, accessed July 2021).

[76] Cypress Semiconductor Corporation. CY8CKIT-059 PSoC 5LP prototyping kit with onboard programmer and debugger. (`www.cypress.com`, accessed July 2021).

[77] Texas Instruments. FDC1004Q 4-channel capacitance-to-digital converter. (`www.ti.com/FDC1004-Q1`, accessed July 2021).

[78] RS Components. 10 pin female SOP to 10 pin male DIP adapter. (`www.it.rs-online.com`, accessed July 2021).

[79] Texas Instruments. μA78Mxx positive-voltage regulators. (`www.ti.com/UA78M`, accessed July 2021).

[80] SparkFun Electronics. Sparkfun logic level converter - bi-directional. (`www.sparkfun.com`, accessed July 2021).

[81] K. Arshak, E. Moore, G. M. Lyons, J. Harris, and S. Clifford. A review of gas sensors employed in electronic nose applications. *Sensor Review*, 24(2):181–198, January 2004.

[82] B. Vercelli, S. Zecchin, N. Comisso, G. Zotti, A. Berlin, E. Dalcanale, and L. "Bert" Groenendaal. Solvoconductivity of polyconjugated polymers: The roles of polymer oxidation degree and solvent electrical permittivity. *Chemistry of Materials*, 14(11):4768–4774, 2002.

[83] Cypress Semiconductor Corporation. AN70698 - PSoC 3, PSoC 4 and PSoC 5LP temperature measurement with an RTD. (`www.cypress.com/AN70698`, accessed July 2021).

[84] Cypress Semiconductor Corporation. AN58827 - PSoC 3 and PSoC 5LP internal analog routing considerations. (`www.cypress.com/AN58827`, accessed July 2021).

[85] Wavetek Meterman. 16XL digital multimeter. (`www.tequipment.net`, accessed August 2021).

Ringraziamenti

Sono dunque arrivato alla conclusione di un altro capitolo della mia vita, e vorrei dedicare qualche parola a coloro che mi hanno accompagnato, seguito, aiutato, sopportato nel viaggio.
Innanzitutto ringrazio il mio relatore Pietro Cerveri, che mi ha offerto la possibilità di lavorare a questo progetto e ha riposto fiducia nelle mie capacità proponendomi di continuare la mia crescita con un percorso di dottorato. Ringrazio di cuore Davide Marzorati, che nel corso di questi sei mesi è stata la mia guida sul campo ed ha sempre trovato un momento da dedicarmi. Ci tengo a ringraziare anche il Professor Francesco Cellesi e Francesco Bosatelli per l'ottimo lavoro svolto assieme e la disponibilità dimostrata durante la collaborazione.
Un enorme grazie va alla mia famiglia: mia mamma, mio papà, i miei due fratelli, i miei nonni e i miei parenti più stretti, per aver sempre creduto in me, gioito per i miei successi e non avermi mai fatto mancare nulla nei momenti meno facili.
Ringrazio i miei amici della Bassa, compagni di vita nella buona e nella cattiva sorte: Eleonora, Federico, Irene e Stefano. Non riesco ad immaginarmi qui, ora, senza pensare a tutte le esperienze fatte assieme nel corso degli anni.
Ringrazio la mia amica più sincera: Giulia, che dal primo giorno in cui si è trasferita nella nostra classe del liceo ha instaurato con me un rapporto che spero di non perdere mai, e tutta la sua famiglia, che nel tempo è diventata un po' una seconda casa. Ringrazio Luca ed Edoardo, compagni di lunghe serate passate ad esplorare ogni tipo di gioco da tavolo. Ringrazio Silvia, amica sempre presente dai tempi delle scuole medie.
Un ringraziamento va anche ai membri della mia band, gli Effetto Morgana: Alberto, Davide, Gianluca e Luigi, per tutte le ore passate a divertirci in sala prove e per quelle (purtroppo poche) serate in cui ci siamo esibiti dal vivo. Ringrazio anche Andrea, mio fedele maestro e amico.
Infine, non posso non ringraziare tutti coloro che ho avuto il piacere di conoscere durante questi cinque, lunghi anni di università, e coi quali ho condiviso gioie e sofferenze: Beatrice, Damiano, Elena, Fabio, Federico, Michele, Oswaldo, Piergiorgio, Rodolfo e Simon. Grazie per aver reso tutto un po' più leggero.